

JGR Solid Earth

L

RESEARCH ARTICLE

10.1029/2025JB032593

Key Points:

- We estimated anisotropic Skempton's coefficients under triaxial conditions
- Radial coefficient increases and axial coefficient decreases with increasing load
- Axial coefficient appears negative at high load, beyond the point of net dilation

Correspondence to:

N. Brantut, nicolas.brantut@gfz.de

Citation:

Elsigood, B., Brantut, N., Meredith, P. G., & Mitchell, T. M. (2025). The undrained response of Westerly granite subjected to cyclical changes in load. *Journal of Geophysical Research: Solid Earth, 130*, e2025JB032593. https://doi.org/10.1029/2025JB032593

Received 29 JUL 2025 Accepted 23 OCT 2025

Author Contributions:

Conceptualization: Bobby Elsigood, Nicolas Brantut, Philip G. Meredith, Thomas M. Mitchell Data curation: Bobby Elsigood Formal analysis: Bobby Elsigood, Nicolas Brantut Investigation: Bobby Elsigood, Nicolas Brantut

Methodology: Bobby Elsigood, Nicolas Brantut Project administration: Philip

Project administration: Philip G. Meredith

Resources: Nicolas Brantut, Philip G. Meredith

Software: Bobby Elsigood, Nicolas Brantut

Supervision: Nicolas Brantut, Philip G. Meredith, Thomas M. Mitchell Validation: Bobby Elsigood, Nicolas Brantut

Visualization: Bobby Elsigood, Nicolas Brantut

Writing – original draft: Bobby Elsigood, Nicolas Brantut

© 2025. The Author(s).

This is an open access article under the terms of the Creative Commons

Attribution License, which permits use, distribution and reproduction in any medium, provided the original work is properly cited.

The Undrained Response of Westerly Granite Subjected to Cyclical Changes in Load

Bobby Elsigood¹, Nicolas Brantut^{1,2}, Philip G. Meredith¹, and Thomas M. Mitchell¹

¹Department of Earth Sciences, University College London, London, UK, ²GFZ Helmholtz Centre for Geosciences, Potsdam, Germany

Abstract When subjected to changes in applied stress, the pore space of rocks elastically deforms, producing changes in internal pore pressure when the pore fluid is unable to flow in or out of the stressed volume. The magnitude of this effect depends on the geometry and compliance of the pore space, which is a function of the overall microcrack population within the rock. To test how increasing levels of stress-induced microcracks impact the poroelastic properties of rocks, we measured experimentally the incremental changes of pore pressure in response to small increments of axial and radial stress (i.e., Skempton coefficients) in Westerly granite at increasing differential stress under triaxial conditions. The anisotropy in loading conditions, with increasing differential stress at constant pressure, leads to anisotropy in poroelastic properties. With increasing load, the apparent Skempton coefficient in the axial direction decreases, while the apparent Skempton coefficient in the radial direction increases. At a stress level commensurate to that at the onset of dilatancy dominance, the apparent axial Skempton coefficient becomes negative, that is, local pore pressure increases in response to decreases in axial stress. Upon unloading, we observe hysteresis in both coefficients, with the axial one remaining lower in the unloading path than in the loading path. The negative Skempton effect in highly stressed rocks implies that pore pressure might locally increase around faults experiencing rapid unloading, for example, during earthquakes.

Plain Language Summary When rocks are squeezed or stretched, the microscopic cracks and pores within them are deformed and change volume. When these cracks and pores are filled with a fluid (water, gas, etc.), their volume change lead to change in fluid pressure. We typically expect that squeezing the rock leads to fluid pressure increase. We detected this effect experimentally in granite, and examined how its magnitude varied with increasing deformation and cracking of the rock. We found that the change of fluid pressure depended strongly on the direction of loading. When the rock was brought to high loads, the increased population of cracks aligned with the loading direction lead to a reversal of the anticipated effect: squeezing the rock in the direction parallel to the cracks lead to small but detectable decreases in fluid pressure. This reversal might be important to the understanding of how rocks respond to sudden deformation such as those occurring near faults during earthquakes.

1. Introduction

Void spaces (pores and cracks) in rocks are often saturated with a pressurized fluid, so that any change in the volume of the void space can potentially result in a change in the fluid pressure (e.g., Jaeger et al., 2007, chap. 7). When the stresses applied to a rock mass vary suddenly, for example, during an earthquake, the instantaneous response of the rock is initially undrained, that is, fluid is macroscopically immobile and fluid pressure evolves following local pore volume change. Over time, the pressure variations are relaxed due to fluid diffusion. In isotropic, linear elastic materials, the fluid pressure change associated with a sudden (undrained) stress change is characterized by Skempton's coefficient, which is defined as the ratio of pore pressure to mean stress change (e.g., Wang, 2000, Section 2.4). This coefficient is usually positive: a compressive increment in mean stress leads to an incremental increase in pore pressure. This phenomenon was generalized by Skempton (1954) to include the possibility that shear stresses also produce pore pressure changes. In anisotropic materials, more coefficients are required to describe the undrained behavior: we expect the pore pressure change to be different depending on the direction of the stress increment with respect to the symmetry axes of the material (e.g., Wang, 2000, Section 2.7).

One major source of anisotropy in rock physical properties (elastic and transport) is the preferred orientation of microcracks (e.g., Walsh, 1965b), which is the result of either pre-existing structures from rock formation

ELSIGOOD ET AL. 1 of 23

10.1029/2025JB032593

Writing – review & editing: Nicolas Brantut, Philip G. Meredith, Thomas M. Mitchell processes, or from anisotropic stresses preferentially closing or opening microcracks. Under conventional triaxial conditions (with principal stresses such that $\sigma_1 > \sigma_2 = \sigma_3$) and at low temperature (in the brittle regime), differential stress induces transverse isotropy in the microstructure, with the axis of symmetry aligned with the maximum compression axis. Initially, an increase in differential stress leads to the progressive elastic closure of pre-existing microcracks which are aligned perpendicularly to the direction of maximum compression (Lockner & Byerlee, 1977). As samples undergo further increases in differential stress, new tensile microcracks nucleate and grow in a direction parallel to the compression axis (Paterson & Wong, 2005, Chapter 5). This damage is dilatant, where progressive increases in compressive stress result in an increase in sample volume (Brace et al., 1966). When the rock is fluid-saturated and under undrained conditions, we also expect a concomitant pore pressure decrease (Brace & Martin, 1968).

Decreases in differential stress reverse this process and lead to changes in volumetric strain by forcing the closure of the new tensile microcracks and the reopening of the pre-existing ones. However, changes in volumetric strain do not necessarily follow the same path during these increases and decreases in differential stress. Instead, they produce hysteresis loops that are generally reversible during repeated cycles to the same maximum differential stress (Scholz & Kranz, 1974; Zoback & Byerlee, 1975a). Furthermore, once the previous maximum stress has been exceeded, new hysteresis loops are observed (Brantut & Petit, 2023; Holcomb, 1981). This stress history dependence has also been observed in other physical properties, such as wave velocities (e.g., Brantut & Petit, 2023; Holcomb, 1981; Passelègue et al., 2018) and permeability (e.g., Mitchell & Faulkner, 2008; Zoback & Byerlee, 1975b). Therefore, physical properties and anisotropy of rocks depend on both the state of stress and the stress history, which together control the state of the material microstructure.

In low-porosity rocks such as granite, changes in volumetric strain are dominated by the opening and closing of cracks, which depend on both the stress and the stress history. Rapid changes in pore volume (e.g., from cracks opening and closing) cause changes in pore pressure due to poroelastic coupling. In the course of loading-unloading cycles under triaxial conditions, the undrained poroelastic parameters, and in particular the Skempton coefficients, are expected to be anisotropic, and to vary with stress due to evolving anisotropy in the material fabric. However, in situ measurements of pore pressure changes under undrained conditions are notoriously difficult due to the interaction between the pore space of the rock and the drainage system (pore fluid piping). The influence of the drainage system is particularly noticeable for "tight" rocks because of their very low pore volume (Ghabezloo & Sulem, 2010).

Early experimental indications of anisotropy in Skempton's coefficient was presented in Wang (1997), who reported pore pressure variations in response to uniaxial loading that were lower than anticipated by a purely isotropic theory. Further work conducted on porous sandstone and ceramics indicate the development of stress-induced anisotropy reflected in variations in axial and radial Skempton's coefficients (Lockner & Beeler, 2003; Lockner & Stanchits, 2002), with an overall decrease in axial Skempton's coefficient with increasing overall differential stress under triaxial stress conditions. Pimienta et al. (2015a, 2015b) also report anisotropic poroelastic behavior in porous sandstone, with pore pressure change being lower in response to axial loading than hydrostatic loading.

In contrast to undrained poroelastic constants, elastic wave velocities and their anisotropy have been regularly measured during rock deformation tests, including cycling loading, and can be used to determine microcrack fabric evolution (e.g., Benson et al., 2005; Brantut & Petit, 2023; Passelègue et al., 2018; Sayers & Kachanov, 1995; Schubnel et al., 2003). In a recent theoretical development, Wong (2017) established a link between the microcrack fabric parameters that can be obtained from wave velocity data and the undrained moduli of water-saturated cracked rocks. The model of Wong (2017) relies on the combination of an effective medium model for cracked, dry materials (Sayers & Kachanov, 1995), and the use of a micromechanical model to arrive at undrained moduli and undrained coefficients (A. H.-D. Cheng, 1997). This approach has the potential to dramatically simplify the estimation of undrained parameters in rocks, and possibly open the way for field estimates based on seismic data. However, it relies on many assumptions regarding microcrack geometry and homogeneity of the solid, and its use with seismic or ultrasonic data is also questionable due to the possibly large differences between static and dynamic moduli (even in dry rocks). Recently, Elsigood et al. (2023) showed that Wong (2017)'s model could adequately predict the anisotropy in Skemption coefficients in thermally cracked Westerly granite under triaxial conditions, but quantitative agreement was quite limited, especially at low pressure. Further testing of the model and its limitations is thus warranted.

ELSIGOOD ET AL. 2 of 23

21699356, 2025, 11, Downloaded from https://agupubs.onlinelibrary.wiley.com/doi/10.1029/2025JB032593 by Nicolas Brantut

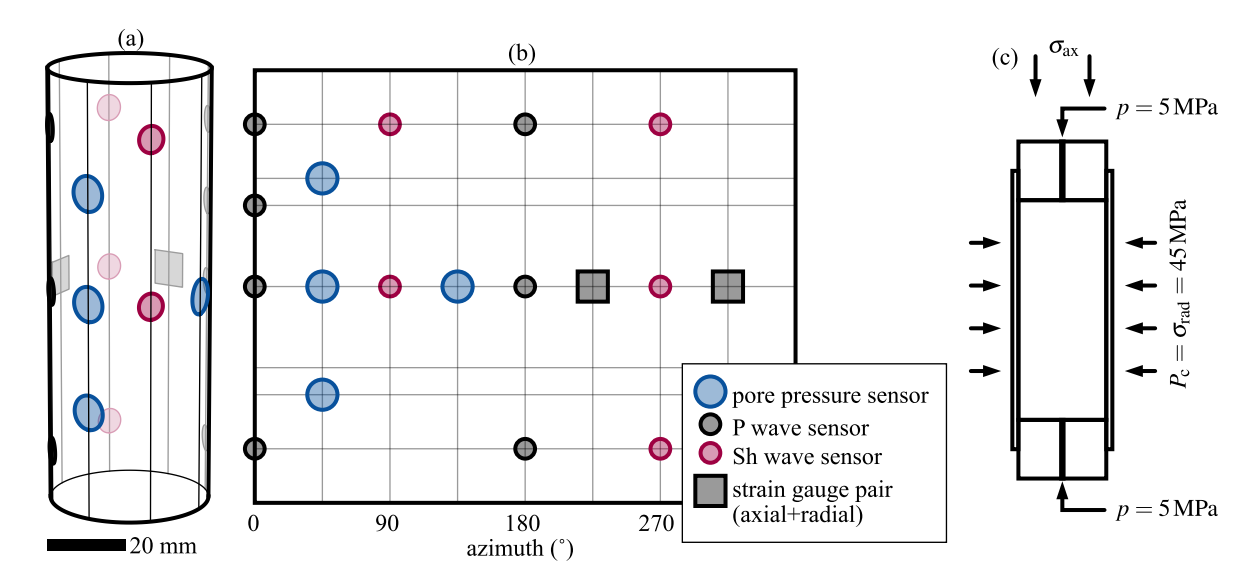


Figure 1. (a) Schematic of sensor arrangement and (b) full map of all sensors in contact with the cylindrical surface of the sample. (c) Loading geometry and boundary conditions.

Here, we present results from experiments designed to obtain in situ measurements of pore pressure change due to rapid axial and radial stressing in water-saturated Westerly granite. Conventional experimental methods in poroelasticity typically require undrained boundary conditions at the sample scale, which would imply impracticably large errors and corrections for low-porosity rocks like granite (e.g., Lockner & Stanchits, 2002, §9). Thus, we use here an alternative method based on transient measurements, relying on the rather long hydraulic diffusion timescale across our sample to capture the initial (transient, local) undrained pore pressure changes. We interpret our data in terms of anisotropic apparent Skempton coefficients, keeping in mind that we cannot access the true static undrained properties of the overall sample. These measurements were repeated at selected stress states during increasing amplitude cyclic loading. In the same experiments, we also measured elastic wave velocities, and estimate the evolution in microcrack fabric parameters with changing stress conditions (following Shafiro & Kachanov, 1997; Schubnel et al., 2003). We extrapolate these dynamic parameters to low frequency, undrained quantities, and compare the predicted Skempton coefficients with those measured directly.

2. Experimental Method

2.1. Testing Apparatus and Sample Instrumentation

Experiments were conducted on a cylindrical sample of Westerly granite of 100 mm length and 40 mm diameter. The sample was equipped with two pairs of axial and radial strain gauges, located around the center. The sample was jacketed in a perforated nitrile sleeve, and 12 ultrasonic transducers and three fluid pressure sensors were positioned around the surface of the cylinder (Figure 1a).

Seven of the ultrasonic transducers were polarized perpendicularly to the sample surface (and thus mostly sensitive to incoming P-waves), and five transducers were polarized tangentially to the surface, in the horizontal direction (and thus sensitive to incoming Sh-waves). The 12 transducers were arranged around the sample so that straight rays connecting P-wave sensitive sensors were at five different angles from the sample vertical axis, and rays connecting Sh-wave sensitive sensors were at three different angles from the sample axis (Figure 1b).

The fluid pressure sensors are made of a stainless steel stem with a 0.4 mm diameter hole in direct contact with the sample surface at one end, and connected to a thin penny-shaped cavity (0.2 mm thick, 7 mm in diameter) at the other end. The cavity is closed with a sealed steel cap mounted with a diaphragm strain gauge that is sensitive to the difference between the pressures on either side, that is, confining pressure on the outside and pore fluid pressure on the inside. Details of the design and calibration of the sensors can be found in Brantut (2020) and Brantut and Aben (2021). Three such sensors were placed on the sample surface in line at different positions along

ELSIGOOD ET AL. 3 of 23

the sample vertical (a quarter, half, and three quarters from the sample ends; Figure 1b). Only the middle sensor was used for calculations as this furthest position from the sample ends maximizes the time under undrained conditions.

The jacket was sealed with epoxy around each sensor, and the sample was placed in the conventional, oil-medium triaxial apparatus installed in the Rock and Ice Physics Laboratory at UCL (Eccles et al., 2005). All tests were conducted at room temperature. Confining pressure was set by a hand pump and adjusted manually throughout the test. It was recorded at the pressure vessel inlet by a pressure transducer. Axial load was applied by an autocompensated piston driven by a servo-hydraulic ram, and measured using an internal load cell. Axial shortening was measured by an external linear variable differential transformer, corrected for the calibrated machine stiffness.

The pore fluid system was connected to both the top and bottom of the sample, and grooved steel disks distributed the fluid across the sample end surfaces. Pore fluid pressure was controlled using a servo-hydraulic intensifier. All mechanical data were acquired at a frequency of up to 5 Hz.

At regular intervals, wave velocity surveys were conducted, where a 250 V 1 MHz pulse was sent from and to each of the P- and Sh-wave transducers in turn. The collected waveforms were analyzed using a cross-correlation method (e.g., Brantut, 2015) to obtain accurate relative variations in P- and Sh-wave velocities throughout the experiment. The absolute accuracy of wave velocity measurements was impacted by the manual picking of a reference data set, by additional errors due to imperfect coupling between sensors and the rock surface, and by the overall low aperture of the ultrasonic sensors (e.g., Kovalyshen et al., 2020). The resulting error is of the order of ± 150 m/s, estimated by manual exploration of possible picks.

2.2. Experimental Protocol

Throughout the experiment, confining pressure was maintained nominally constant at 45 MPa and the sample was saturated with water held at a controlled pore pressure of 5 MPa (Figure 1c). Permeability was measured prior to deformation using the steady-state flow method with pore pressure controlled at 5 MPa at one end of the sample and vented at the other. At 10 MPa confining pressure, permeability was 1.3×10^{-19} m², and at 45 MPa confining pressure, permeability was 6.1×10^{-21} m².

There were two main features of the experimental protocol: (a) increasing amplitude (hundreds of MPa) differential stress cycles; and (b) repeated small-amplitude (a few MPa) rapid strain-rate (greater than 10^{-4} s^{-1}) radial and axial stress cycles. The large amplitude stress cycles were performed to introduce and recover (at least in part) increasing levels of anisotropy and damage in the sample. The rapid stress cycles were conducted to measure how (transiently) undrained strain and pore pressure changes evolved due to this damage.

The following sequence of large amplitude stress cycles was chosen (Figure 2a): Starting from 20 MPa differential stress (cycle 0), we first increased differential stress up to 220 MPa (cycle 1), then unloaded, reloaded up to 345 MPa, and unloaded again to 20 MPa (cycle 2) and repeated the operation to reach 440 MPa (cycle 3). Finally, the sample was brought to failure (not shown in Figure 2) to measure its strength, which was 520 MPa.

The rapid axial and radial stress changes were conducted at nine selected stress levels during the large amplitude loading cycles (Figure 2a). At each level, axial and radial stress were independently and repeatedly stepped up and down. Following each change in stress, it was necessary to allow sufficient time for the pore pressure in the sample to equilibrate due to the low hydraulic diffusivity of the granite. The typical timescale required for reequilibration of pore pressure after a stress step was of the order of 1,000 s, consistent with a hydraulic diffusivity of the order of 10^{-5} m²/s. The rapid step changes in axial stress were up to 7 MPa and the changes in confining pressure were of around 1 MPa.

The quantity of measurements conducted resulted in the experiment taking over 1 month to complete.

2.3. Estimations of Apparent Undrained Parameters

Conventional measurements of undrained quantities require that the tested sample is under undrained boundary conditions, that is, no fluid flow in an out of the specimen, and that pore pressure is homogeneous at the sample scale. In practice, experiments are often conducted under "experimentally undrained" conditions (Pimienta

ELSIGOOD ET AL. 4 of 23

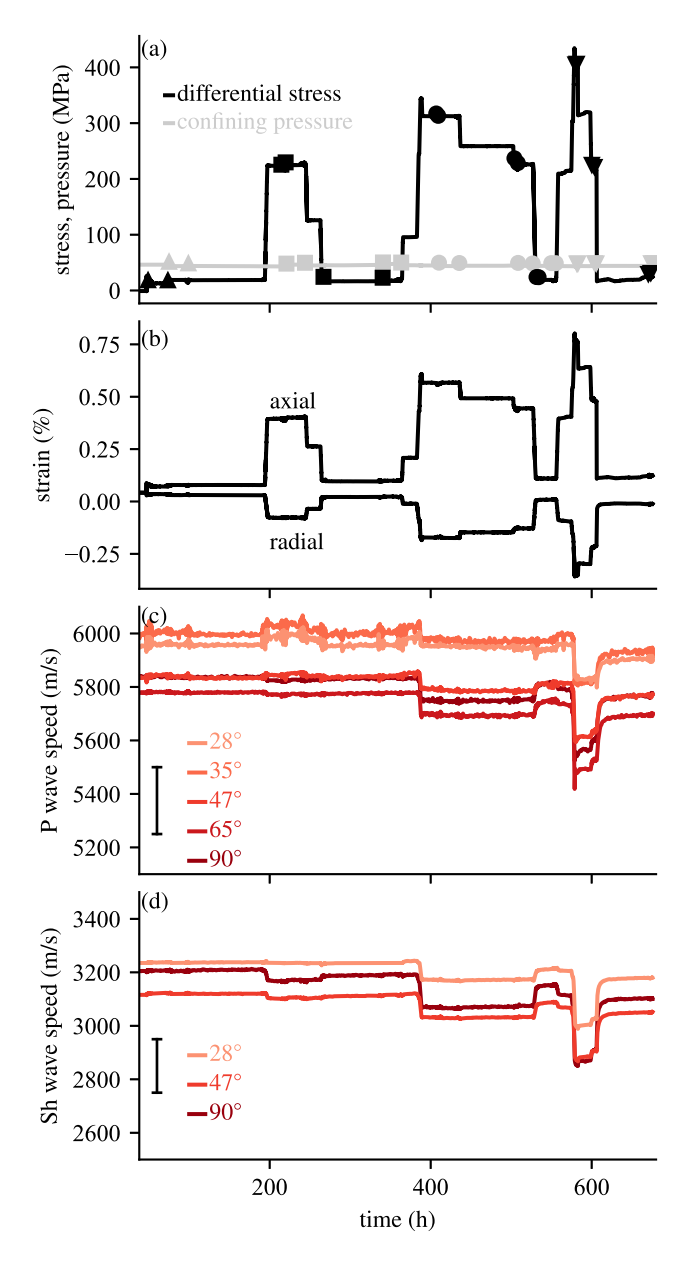


Figure 2. Time series of differential stress, confining pressure (a), axial and radial strain (b), P-wave (c), and Sh-wave velocities (d) for the entire duration of the test. The markers indicate when low amplitude stress steps were conducted: triangle up (\triangle) is for cycle 0, squares (\square) are for cycle 1, circles (\bigcirc) are for cycle 2, and triangles down (∇) are for cycle 3.

et al., 2016), that is, with a non zero dead volume in the pore fluid lines upstream and/or downstream the sample itself. This additional dead volume needs to be corrected for (or artificially suppressed, as in Lockner and Stanchits (2002)) to estimate Skempton's coefficients. While such corrections are feasible for porous rocks, whereby the pore volume may not be small compared to the dead volume, for low porosity cracked rocks the correction would be large and conducive to large errors. Here, we develop an alternative measurement methodology that allows us to measure Skempton's coefficients in a transient manner. Because of the assumptions of the method and to avoid confusion with conventional techniques, we subsequently call our measurements "apparent" undrained quantities (in the same way as Pimienta et al., 2015b, called their results "pseudo-"Skempton coefficients).

We imposed constant rate (servo-controlled ramp) changes in axial stress and step changes (manual pump) in radial stress and measured the resulting changes in pore pressure and axial and radial strain. Since the imposed stress changes occurred over a much shorter timescale (a few seconds) than the hydraulic diffusion timescale across the sample (around 1,000 s), the initial response of the sample is expected to be transiently undrained. Pore pressure was maintained constant at both ends of the sample, so that internal pore pressure gradually reequilibrated over time due to drainage.

Assuming uncoupled poroelastic response and diffusion along the sample axis z, the spatiotemporal evolution of pore pressure in the sample is given by a diffusion equation (e.g., Pimienta et al., 2016)

$$\frac{\partial \Delta p}{\partial t} - \alpha \frac{\partial^2 \Delta p}{\partial z^2} = \frac{1}{3} B_i \frac{\partial \Delta \sigma_i}{\partial t},\tag{1}$$

where Δp is the pore pressure change, t is time, α is hydraulic diffusivity, B_i is the Skempton coefficient along direction i (as defined in Wang, 2000, Section 2.7) and $\Delta \sigma_i$ is the (imposed) stress change along direction i (i = x, z). The solution of Equation 1 subject to boundary conditions $\Delta p = 0$ at $z = \pm L$, and for an initial step change in stress producing an undrained pressure change $\Delta p_{\text{undrained}} = B_i \Delta \sigma_i / 3$ is (Carslaw & Jaeger, 1959, Section 3.4):

$$\Delta p(z,t) = \Delta p_{\text{undrained}} \frac{4}{\pi} \sum_{n=0}^{\infty} \frac{(-1)^n}{2n+1} e^{-(2n+1)^2 \pi^2 (t/t_{\text{diff}})/4} \cos \frac{(2n+1)\pi z/L}{2}, \quad (2)$$

where $t_{\text{diff}} = L^2/\alpha$ is the hydraulic diffusion time, and L is the sample's half-length.

For our granite sample with low hydraulic diffusivity, $t_{\rm diff}$ was of the order of 1,000 s, so that the peak local pore pressure change measured in the centermost portion of the specimen should be representative of the undrained

response (Figure 3). The validity of this measurement method relies on two factors: (a) homogeneity of the sample, and (b) fast sensor response time compared to overall diffusion time.

There is no indication that our Westerly granite sample was significantly heterogeneous before deformation, and we only increased the applied differential stress up to 85% of the failure stress. Even at the highest applied stress (cycle 3), we did not detect substantial deviations between the local strains measured by strain gauges. In addition, strain localization in granite typically appears at stresses larger than 85% of the peak (e.g., Aben et al., 2018; Lockner et al., 1991; McBeck et al., 2022). Therefore, the specimen can be considered homogeneous throughout the experiment.

ELSIGOOD ET AL. 5 of 23

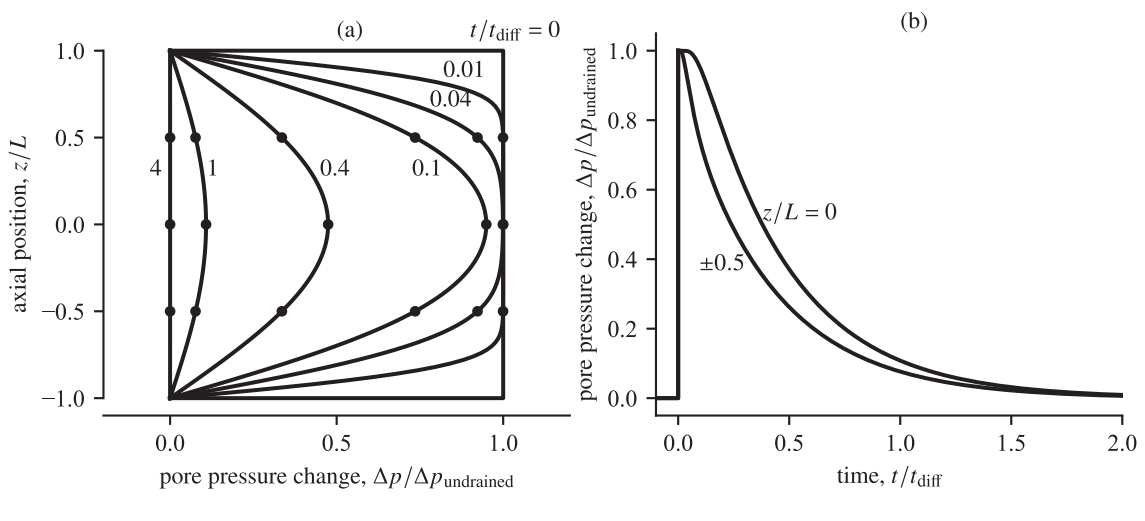


Figure 3. Simulation of the spatiotemporal evolution of pore pressure in the sample following an initial homogeneous step increment $\Delta p_{\text{undrained}}$. The sample's half-length is denoted L, z is the axial position, t is time, and t_{diff} is the hydraulic diffusion time. Pore pressure change is maintained at zero at both ends of the sample. (a) Snapshots of pore pressure profiles; filled circles indicate transducer positions in our experimental setup. (b) Time evolution of pore pressure at three positions along the sample $(z/L = 0 \text{ and } z/L = \pm 0.5)$. In our experiment, L = 50 mm and t_{diff} is of the order of 1,000 s.

A more challenging aspect of the measurements is the delayed detection of pore pressure transients due to the existence of a small fluid-filled cavity within the transducers that leads to a time-dependent fluid exchange between the rock and the transducer (Brantut & Aben, 2021). Even under experimentally undrained conditions, the existence of dead volumes in pore fluid instrumentation and tubing leads to delays and limits the amplitude of pore pressure measurements (e.g., Pimienta et al., 2015b; Pimienta et al., 2016). In particular, under oscillatory stress variations, delays in pore pressure equilibration between sample and sensing elements lead to phaseshifts and to apparent negative values of poroelastic coefficients (Pimienta et al., 2015b). Here, we imposed stress steps and waited for sufficiently large time for pore pressure transients to dissipate between each step, so our measurements should not be impacted by phase shifts. However, the amplitude of pore pressure changes are impacted by the delay, since pore pressure in the sample gradually decreases due to drainage at the boundaries.

As an example of transducer response time, Figure 4 shows that the maximum pore pressure change in the center of the sample occurred around 180 s after an imposed differential stress change that occurred over around 6 s. Note that a similar delayed response was noted by Hart and Wang (2001), who were unable to determine the cause. This delay limits our ability to capture precisely the true transient undrained response. Therefore, our estimate of Skempton's coefficients must be considered a lower bound. Pore pressure measured off the center, at positions $z = \pm 25$ mm (see Figure 1), show a lower maximum variation after the initial delay, which is consistent with the prediction shown in Figure 3. We also note that there is some variability in each transducer response time, which could be due to local variations in hydraulic properties. As stated above, we will only use the transducer positioned centrally to record the maximum pore pressure change and limit the effects due to the delayed response.

The error could be severe if the hydraulic diffusion time across the sample $(t_{\rm diff})$ were commensurate or shorter than the transducer delay time. This is not the case: the transducer response time is given by $t_{\rm trans} = \beta_{\rm trans}^2/(\beta^2A^2\alpha)$, where $\beta_{\rm trans}$ is the transducer storage capacity, β is the rock storage capacity and A is the transducer-rock contact area (Brantut & Aben, 2021). Due to the small dimensions of the transducer compared to the sample's half-length L, the ratio $t_{\rm trans}/t_{\rm diff}$ is always much smaller than 1 (using transducer parameters given in Brantut & Aben, 2021). In the example of Figure 4, the transducer response time was of the order of 100 s, which is 10 times smaller than $t_{\rm diff}$. In that example, it took over 1 hour for pore pressure to return to the 5 MPa value imposed at the boundaries.

In our pressure vessel with a compensated piston, changes in confining pressure should in principle lead to an isotropic response. However, the early response is essentially that of an increase in radial stress only due to a combination of the piston seal friction, time taken for confining oil to reach the compensation chamber and realignment of the piston. Our records of internal load indicate that there are small changes in axial stress relative

ELSIGOOD ET AL. 6 of 23

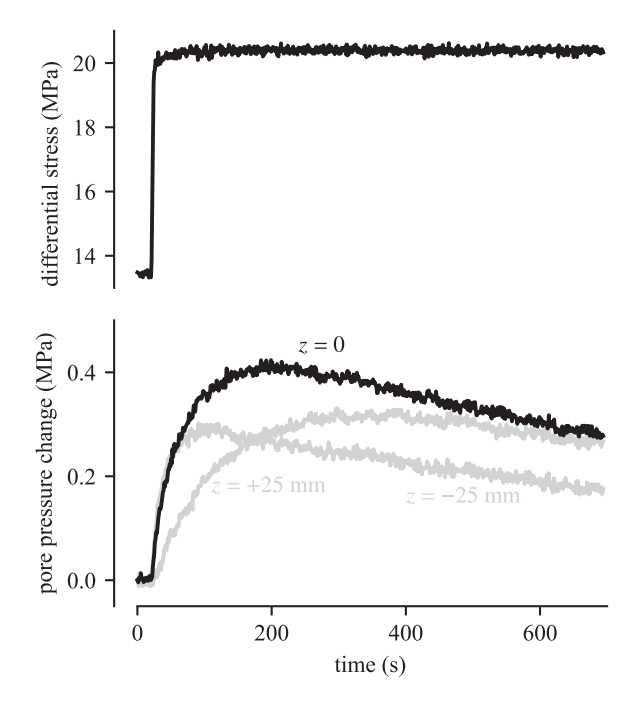


Figure 4. An example of the delayed pore pressure sensor response to changes in axial stress. Here, pore pressure would only be expected to increase during increases in stress, however this is delayed due to the nonzero dead volume inside fluid pressure sensors. Pore pressure measured in the central portion (z=0) increases more than that measured above and below $(z=\pm 25 \text{ mm})$.

to the changes in confining pressure steps. Whilst the small changes in axial stress do influence the pore pressure response through the Skempton effect, the effect of radial stress changes dominates and hence, in our calculations, we have assumed purely radial stress changes (see Appendix A).

The strain gauges that were bonded directly on to the sample surface recorded the instantaneous changes in axial and radial strain in response to changes in axial stress. Undrained Young's modulus and undrained Poisson's ratio were calculated from the linear fit (least-squares) of axial and radial strain against axial stress.

The radial and axial Skempton coefficients were calculated as (Wang, 2000, Section 2.7) $B_x = 3\Delta p/2\Delta\sigma_x$, $B_z = 3\Delta p/\Delta\sigma_z$, where Δp is the change in pore pressure, $\Delta\sigma_x = \Delta\sigma_y$ is the change in radial stress, and $\Delta\sigma_z$ is the change in axial stress. We calculated the Skempton coefficients by taking the maximum change in pore pressure following a change in external stress.

2.4. Inferring Crack Density Tensors and Undrained Coefficients From Ultrasonic Data

One of our objectives was to determine the extent to which wave velocity data can be used to infer poroelastic quantities such as Skempton's coefficients. To make any such inference, a number of steps and assumptions are involved (depicted in Figure 5). First, we used a noninteractive effective medium model for fluid-saturated penny-shaped cracks in an homogeneous isotropic matrix (M. Kachanov, 1993) to relate components of the compliance tensor to crack density tensors α_{ij} and β_{ijkl} and saturation parameter ψ^{sat} (see formal definitions below). The elastic compliances in that model are so-called "unrelaxed" because they are derived without regards for fluid pressure equili-

bration between cracks (e.g., Guéguen & Kachanov, 2011; Le Ravalec & Guéguen, 1996; Schubnel et al., 2003). Second, following the steps outlined in Schubnel and Guéguen (2003), the saturation parameter ψ^{sat} is then corrected to simulate the same microcrack fabric but without fluid, ψ^{dry} , hence producing a prediction for the dry (or, equivalently, drained) effective compliance tensor of the material. In a third step, we use the estimated dry compliances to predict properties under undrained conditions (i.e., assuming uniform fluid pressure within the rock representative elementary volume) and obtain Skempton's coefficients B_x and B_z (A. H.-D. Cheng, 1997).

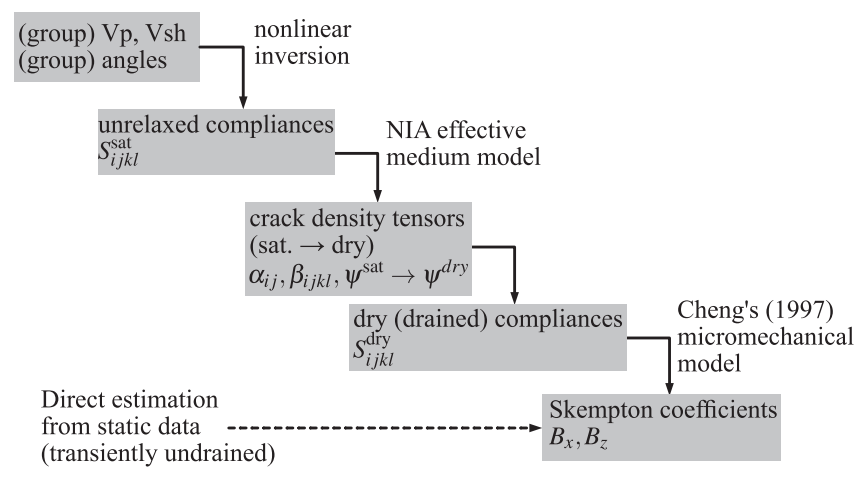


Figure 5. Key steps involved in indirect estimations of Skempton's coefficients from ultrasonic wave velocity data. The underlying principle originates from the work of Schubnel and Guéguen (2003) (estimation of dry compliances from high frequency, fluid saturated compliances) and Wong (2017) (estimation of Skempton coefficients from (dry) crack densities).

ELSIGOOD ET AL. 7 of 23

2.4.1. From Velocities to Crack Densities

In practice, the first step is probably the more challenging and prone to errors. In our triaxial deformation geometry, the effective elastic properties are well described by a transversely isotropic symmetry due to the closure of sub-horizontal microcracks and the development of sub-axial microcracks in the direction of the maximum principal stress (e.g., Passelègue et al., 2018; Sayers & Kachanov, 1995; Schubnel et al., 2003). In this symmetry, five independent components of the compliance tensor are required. In the effective medium model of M. Kachanov (1993) employed here, the compliances are linked to five independent components of two crack density tensors α_{ij} and β_{ijkl} as (e.g., Guéguen & Sarout, 2009)

$$S_{1111}^{\text{sat}} = \frac{1}{E_0} + h(\alpha_{11} + \psi \beta_{1111}), \tag{3a}$$

$$S_{3333}^{\text{sat}} = \frac{1}{E_0} + h(\alpha_{33} + \psi \beta_{3333}),$$
 (3b)

$$S_{1133}^{\text{sat}} = -\frac{\nu_0}{E_0} + h\psi \beta_{1133},\tag{3c}$$

$$S_{1212}^{\text{sat}} = \frac{1 + \nu_0}{2E_0} + h \left(\frac{1}{2} \alpha_{11} + \psi \frac{1}{3} \beta_{1111} \right), \tag{3d}$$

$$S_{1313}^{\text{sat}} = \frac{1 + \nu_0}{2E_0} + h \left(\frac{1}{4} (\alpha_{11} + \alpha_{33}) + \psi \beta_{1133} \right), \tag{3e}$$

where

$$h = \frac{32(1 - \nu_0^2)}{3(2 - \nu_0)E_0},\tag{4}$$

$$\psi = \left(1 - \frac{\nu_0}{2}\right) \frac{\delta}{1 + \delta} - 1,\tag{5}$$

and

$$\delta = \frac{\pi \zeta E_0}{4(1 - \nu_0^2)} \left(\frac{1}{K_{\rm fl}} - \frac{1}{K_0} \right),\tag{6}$$

and where E_0 , ν_0 , and K_0 are the intact material Young's modulus, Poisson's ratio, and bulk modulus respectively, ζ is the (average) crack aspect ratio, and $K_{\rm fl}$ is the fluid bulk modulus.

From the compliance tensor given in Equation 3, we compute the stiffness tensor and P and Sh (phase) velocities at any (phase) angle from the symmetry axis (e.g., Thomsen, 1986). Our off-axis measurements (Figure 1) only provide group velocities (and group angles). The overall relationship between the five independent components of the crack density tensors and the observed group velocities is nonlinear, and requires us to further constrain phase angles based on the group (ray) angles. We determine α_{11} , α_{33} , β_{1111} , β_{1133} and β_{3333} as well as phase angles by using an iterative inverse approach, fitting the observed group velocities and group angles with a least-square minimization procedure (similar to that employed in Brantut & Petit, 2023, Section 2.2). We assumed that the Young's modulus of the solid matrix (E_0) was 89 GPa, the Poisson's ratio (ν_0) was 0.22, the bulk modulus of the fluid ($\kappa_{\rm fl}$) was 2.2 GPa, and the crack aspect ratio ($\kappa_{\rm fl}$) was taken as $\kappa_{\rm fl}$ (e.g., Guéguen & Sarout, 2009). We further constrained the inversion by ensuring positivity of all components of the crack density tensors $\kappa_{\rm fl}$ and $\kappa_{\rm fil}$ and $\kappa_{\rm fil}$ and $\kappa_{\rm fil}$ and $\kappa_{\rm fil}$ are constrained the inversion by ensuring positivity of all components of the crack density tensors $\kappa_{\rm fil}$ and $\kappa_{\rm fil}$ are constrained the inversion by ensuring positivity of all components of the crack density tensors $\kappa_{\rm fil}$ and $\kappa_{\rm fil}$ are constrained the inversion by ensuring positivity of all components of the crack density tensors $\kappa_{\rm fil}$ and $\kappa_{\rm fil}$ are constrained the inversion by ensuring positivity of all components of the crack density tensors $\kappa_{\rm fil}$ and $\kappa_{\rm fil}$ are constrained the inversion by ensuring positivity of all components of the crack density tensors $\kappa_{\rm fil}$ and $\kappa_{\rm fil}$ are constrained the inversion by ensuring positivity of all components of the crack density tensors $\kappa_{\rm fil}$ and $\kappa_{\rm fil}$ are constrained to the constrained the

Beyond potential limitations from the model assumptions, the accuracy of the crack density estimates is limited by the absolute errors in the velocity measurements, which are rather large, especially in the off-axis data (see Kovalyshen et al., 2020, for a detailed analysis). Due to the nonlinearity of the problem, it is difficult to estimate errors in crack densities in absolute terms. However, the relative variations in wave velocities are very accurate

ELSIGOOD ET AL. 8 of 23

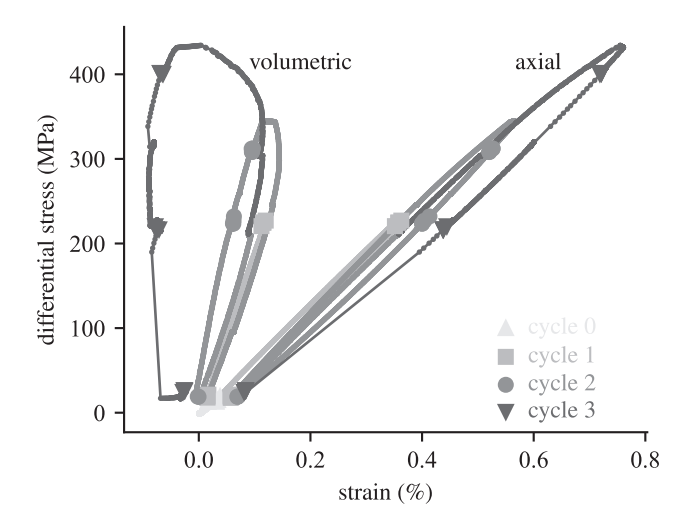


Figure 6. Stress-strain behavior from strain gauge and internal load cell data (gray), and positions where series of small amplitude stress steps were conducted (markers).

due to the cross-correlation procedure employed. Therefore, we anticipate that the relative variations in crack densities are also well constrained.

2.4.2. From Crack Densities to Undrained Properties

Once equipped with estimates of α_{ij} and β_{ijkl} from velocity data, we can use the same effective medium model to predict the compliances in the dry (or, equivalently, drained) limit by considering that the elastic moduli $K_{\rm fl}$ tends to zero. In this case, ψ is equal to $-\nu_0/2$ (close to 0.1), and the influence of the fourth-order crack density tensor β_{ijkl} on the overall crack compliance is thus small (Sayers & Kachanov, 1995).

We follow here the approach of Wong (2017), and compute the drained elastic compliance terms (S_{ijkl}) from Equation 3 with $K_{fl} \rightarrow 0$, from which we calculate the axial and radial Skempton coefficients using the micromechanical relations (A. H.-D. Cheng, 1997)

$$B_x = \frac{3(S_{11} + S_{12} + S_{13}) - 1/K_0}{2S_{11} + 2S_{12} + 4S_{13} + S_{33} + \phi/K_{f1} - (1 + \phi)/K_0},\tag{7}$$

and

$$B_z = \frac{3(2S_{13} + S_{33}) - 1/K_0}{2S_{11} + 2S_{12} + 4S_{13} + S_{33} + \phi/K_{fl} - (1 + \phi)/K_0}.$$
 (8)

Explicit Equations 7 and 8 in terms of crack density tensors are given by Wong (2017).

3. Results

3.1. Behavior During Large Amplitude Stress Cycles

The timeseries of stress, strain and wave velocities are presented in Figure 2, and the corresponding stress-strain behavior is shown in Figure 6. During the first loading cycle (up to 220 MPa differential stress), the sample experienced limited hysteresis and nonlinearity in stress-strain behavior. At 220 MPa differential stress, we observed small increases in subaxial P wave velocities and small decreases in subhorizontal P and Sh wave velocities (by about 20–30 m/s). No significant creep was observed when the sample was left at high stress during this first cycle.

The second loading cycle was conducted up to 344 MPa. At that stress, some time-dependent axial and radial creep strains were measured, and after 1 hr the stress was lowered to 313 MPa. At that load, no further substantial creep strains could be observed. During loading beyond the previous maximum stress, some nonlinearity in axial stress-strain behavior was observed, and volumetric strain showed significant deviations from the initial compression behavior to net dilation above around 300 MPa. After a small increase during loading, the subaxial P wave velocities decreased slightly upon initial unloading and remained constant afterward. By contrast, subhorizontal P and Sh wave velocities decreased by up to 100 m/s during loading, that is, between 1.7% and 3% drop for P and Sh waves, respectively. Upon unloading back to 20 MPa differential stress, the wave velocities returned essentially to their original values. Axial and volumetric strains also returned near their initial values, but significant hysteresis was observed in the stress-strain behavior.

The third loading cycle was conducted up to 435 MPa differential stress. Similarly to the previous cycle, some creep occurred at that stress, and the load was decreased to 400 MPa to limit the time-dependent creep strain accumulation. While differential stress was kept at 400 MPa, no significant axial creep deformation was observed, and limited volumetric creep deformation, of the order of a few tens of µstrain, accumulated. During loading, the volumetric strain showed a large deviation from the initial linear trend, with a net increase in volume compared to the unstressed sample. Upon unloading, the volumetric strain displayed large hysteresis, with almost no change at stresses between 400 and 220 MPa, and a return near the initial, unstressed state at 20 MPa differential stress. The axial strain also displayed large hysteresis in that cycle. The change in P and Sh wave velocities followed a trend

ELSIGOOD ET AL. 9 of 23

21699356, 2025, 11, Downloaded from https://agupubs

onlinelibrary.wiley.com/doi/10.1029/2025JB032593 by Nicolas Brantut -

Helmholtz-Zentrum Potsdam GFZ, Wiley Online Library on [05/11/2025]. See the Term

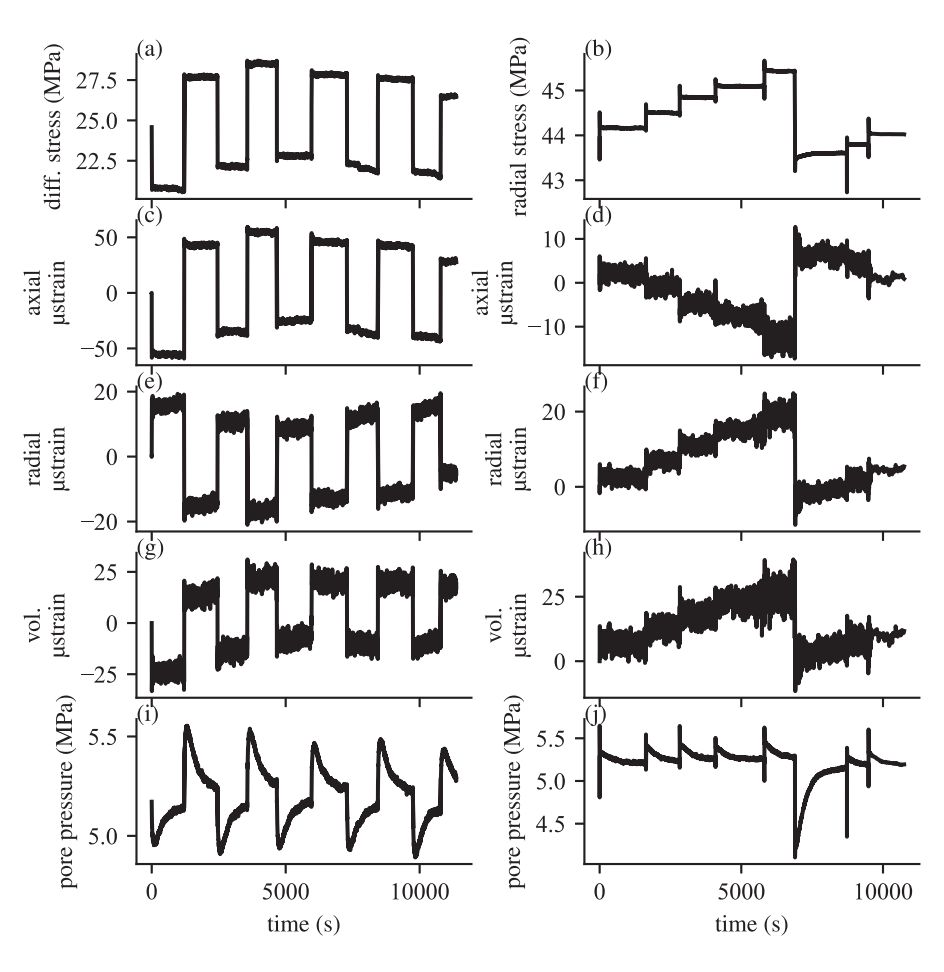


Figure 7. Axial (a) and radial (b) stress changes at low stress (cycle 1) with corresponding changes in axial strain (c, d), radial strain (e, f), volumetric strain (g, h) and pore pressure (i, j). Increases in axial stress lead to increases in pore pressure.

qualitatively similar to that of the previous cycle, with a larger amplitude in the change: the horizontal P wave velocity dropped by about 270 m/s (around 5%) and horizontal Sh wave velocity dropped by about 280 m/s (8.8%). After unloading, the velocities did not return exactly back to their initial, unstressed values.

3.2. Undrained Rapid Axial Stress Cycles

Throughout the experiment, axial stress and confining pressure were independently stepped up and down at nine selected positions during the large amplitude stress cycles. The axial stress and resulting strain and pore pressure changes are shown at two of these positions; first at low stress (cycle 1) in Figure 7, and second at high stress (cycle 3) in Figure 8.

At low differential stress (around 25 MPa, cycle 1), axial stress was rapidly decreased and increased by between 5 and 7 MPa (Figure 7a), causing axial strain decreases and increases of up to 100 µstrain (Figure 7c), increases and decreases in radial strain of around 30 µstrain (Figure 7e), leading to a volumetric strain decreases and increases of around 40 µstrain (Figure 7g). In response to the axial stress decrease, the pore pressure quasi-instantaneously decreased by about 0.4 MPa followed by a slow increase (Figure 7i), and vice versa.

At the highest differential stress (around 400 MPa, cycle 3), axial stress changes were similarly around 5–7 MPa (Figure 8a). For increases in axial stress, axial strain increased by around 80 μ strain (Figure 8c) and radial strain decreased by around 75 μ strain (Figure 8e), which resulted in volumetric strain increasing by around 25 μ strain (Figure 8g). Again, the pore pressure instantaneously decreased by 0.25 MPa and then slowly increased back to its initial value (Figure 8i). A trend of time-dependent decrease in radial and volumetric strain, of the order of 50 μ strain over around 2 hr, was observed in addition to the changes due to the differential stress steps. In another

ELSIGOOD ET AL. 10 of 23

21699356, 2025, 11, Downloaded from https://agupubs.onlinelibrary.wiley.com/doi/10.1029/2025JB032593 by Nicolas Brantut -

Helmholtz-Zentrum Potsdam GFZ, Wiley Online Library on [05/11/2025]. See the Term

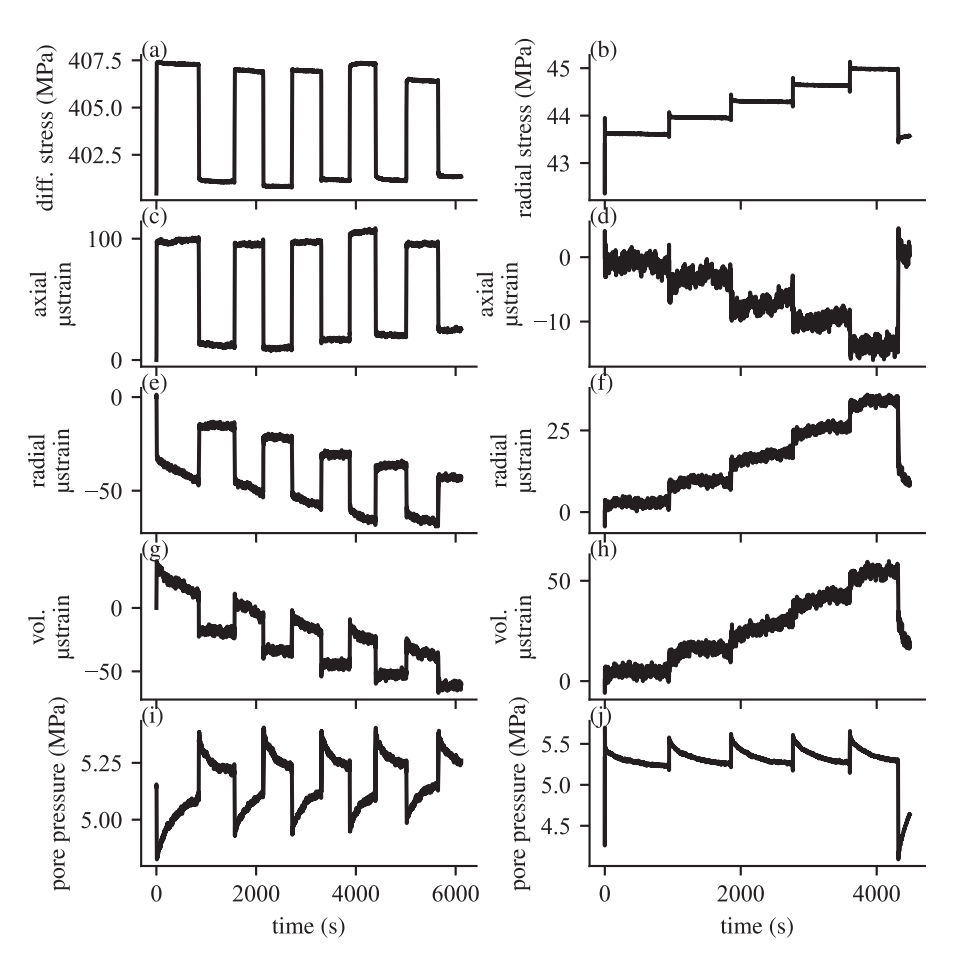


Figure 8. Axial (a) and radial (b) stress changes at high stress (cycle 3) with corresponding changes in axial strain (c, d), radial strain (e, f), volumetric strain (g, h) and pore pressure (i, j). Increases in axial stress lead to decreases in pore pressure.

series of steps conducted during cycle 3 at lower stress (around 220 MPa), a time-dependent trend in radial strain of similar magnitude was also observed but with a drift in the reverse direction.

The major difference between the cycles at high and low differential stress was the change in sign of the pore pressure response. At low differential stress, an increase in axial stress resulted in an increase in pore pressure, whereas at high differential stress an increase in axial stress resulted in a decrease in pore pressure. Volumetric strain remained positive to increases in axial stress even when pore pressure change was negative and therefore the volume of the pore space was increasing whilst the volume of the bulk rock was decreasing.

In contrast with axial stress steps, the response to radial stress steps was qualitatively similar at low and high stress. When radial stress was stepped up, axial strain slightly decreased (indicating axial extension), and radial strain increased, leading to a net increase in volumetric strain (Figures 7 and 8, panels b, d, and h). The resulting pore pressure change was always positive in response to an increase in radial stress.

3.3. Undrained Apparent Elastic Properties

During the series of rapid increases and decreases in axial stress at around 400 MPa, radial strain had an overall decreasing trend with time (Figure 8d). However, this did not affect the short term (undrained) radial responses to stress changes which were reproducible (see Figure 9). For rapid cycles at 400 MPa differential stress, we combined the changes in axial strain during each positive and negative change in stress (Figure 9a). Axial strain changes were linearly increasing with the change in stress with minimal differences between different stress cycles. The same changes in stress also caused changes in radial strain which were linearly decreasing with changes in axial strain and were also reproducible across repeated cycles (Figure 9b). The undrained Young's modulus was calculated from the linear fit between axial stress and axial strain changes (Figure 9a, solid line) and

ELSIGOOD ET AL.

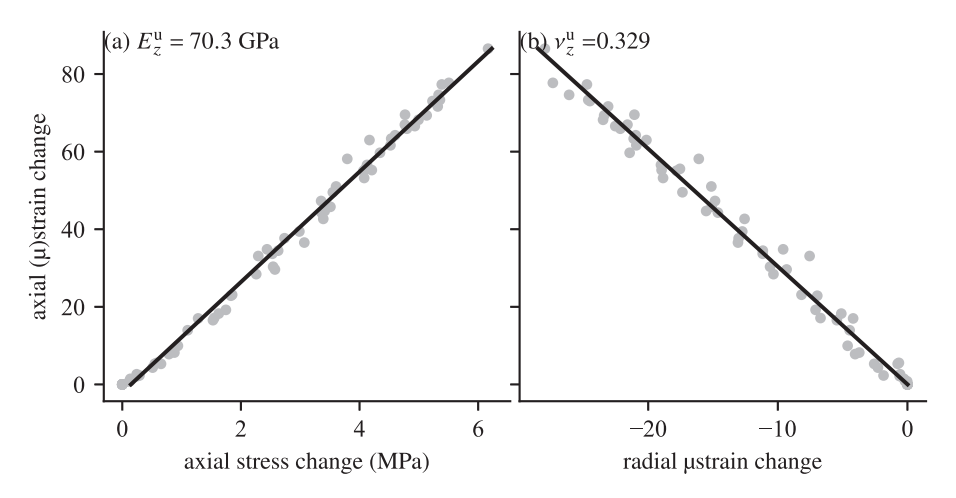


Figure 9. Example of instantaneous poroelastic response at 400 MPa differential stress (cycle 3) in response to step changes in differential stress. (a) Change in axial strain during all increases and decreases in axial stress shown in Figure 8, giving the undrained Young's modulus (E_z^u) . (b) The change in axial and radial strain during the same changes in stress, giving the undrained Poisson's ratio (ν_z^u) .

the undrained Poisson's ratio was calculated from the linear fit between axial strain and radial strain (Figure 9b, solid line).

The undrained Young's modulus and undrained Poisson's ratio were similarly calculated for rapid stress changes at multiple points in the stress history. The full set of results is shown in Table 1. Overall, the undrained Young's modulus was lower at 68.1 GPa at low stress following high stress (Table 1, cycle 3, 26 MPa differential stress) compared with the undrained Young's modulus of 73.6 GPa before the cycles (Table 1, cycle 0, 16 MPa differential stress). However, this trend is not completely clear, because the undrained Young's modulus calculated at low stress for cycle 1 and cycle 2 had greater variation between repeated measurements. The undrained Poisson's ratio is in general higher at higher differential stress. However, similarly to the undrained Young's modulus, the undrained Poisson's ratio calculated during cycle 1 at 18 MPa differential stress and during cycle 2 at 26 MPa differential stress have particularly large variation between repeated measurements.

Table 1Summary of Undrained Poroelastic Parameters (Young's Modulus (E_z^u), Poisson's Ratio (v_z^u), Axial Skempton Coefficient (B_z), and Radial Skempton Coefficient (B_x)) and Their Errors, Calculated From Rapid, Small Amplitude (a Few MPas) Stress Changes Around Nine Values of the Differential Stress ($\sigma_z - \sigma_x$) During the Cyclic Loading Cycles

		$E_z^{\rm u}$, GPa		$ u_z^{ m u}$		B_{x}		B_z	
Cycle	$\sigma_z - \sigma_x$, MPa	Value	SE	Value	SE	Mean	SD	Mean	SD
0	16	73.6	1.01	0.284	0.012	0.71	0.169	0.17	0.02
1	221	74.6	1.02	0.261	0.009	0.76	0.156	0.02	0.003
1	18	74.4	2.87	0.258	0.027	0.69	0.036	0.2	0.029
2	307	74.0	0.91	0.328	0.012	0.78	0.082	-0.05	0.012
2	223	73.6	0.34	0.307	0.003	0.75	0.108	-0.05	0.029
2	20	68.3	3.37	0.314	0.025	0.62	0.12	0.21	0.026
3	404	70.3	0.68	0.329	0.004	1.02	0.134	-0.14	0.009
3	222	69.6	0.42	0.322	0.005	0.94	0.155	-0.08	0.006
3	26	68.1	0.67	0.297	0.007	0.59	0.186	0.17	0.009

Note. Undrained Young's modulus and Poisson's ratio are computed from fitting the slope the stress and strain data (Figure 9), and the standard error (SE) is shown for the fits. The axial and radial Skempton coefficients were separately calculated for each change in pore pressure from a change in stress and the mean and standard deviation (SD) were calculated at each stress level.

ELSIGOOD ET AL. 12 of 23

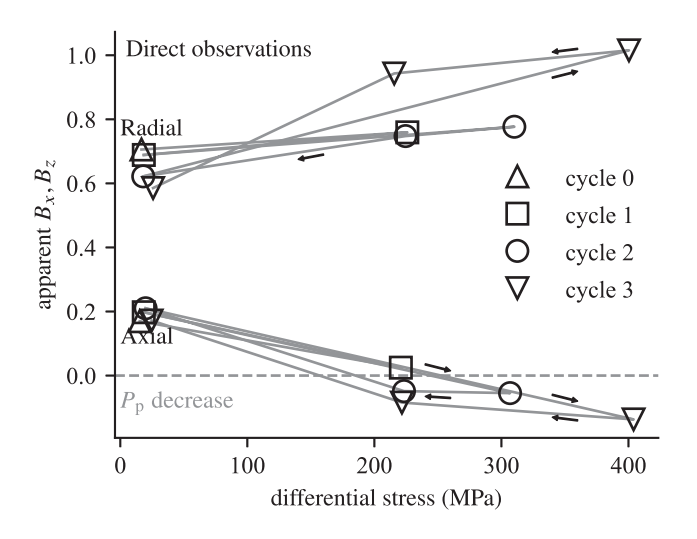


Figure 10. Axial Skempton coefficient (B_z) and radial coefficient (B_x) as a function of differential stress.

3.4. Axial and Radial Apparent Skempton Coefficients

The axial and radial apparent Skempton coefficients were calculated from the ratio of the maximum change in pore pressure from a rapid change in stress. Each measurement was repeated around 10 times and we averaged the results.

The radial Skempton coefficient increased with increasing differential stress (Figure 10). When the large amplitude stress cycles were reversed following a new maximum load, the radial Skempton coefficient decreased with decreasing differential stress, but with some hysteresis.

At low differential stress during cycle 1, the radial Skempton coefficient was around 0.7 (Figure 10, upward triangle). Stress was increased to around 220 MPa and the radial Skempton coefficient increased to around 0.75, and returned to around the initial value when stress was decreased back to 20 MPa (cycle 1, squares). At the maximum differential stress of around 400 MPa during the third cycle (cycle 3, downward triangles), the radial Skempton coefficient reached a maximum of around 1.0.

The trend observed in the axial Skempton coefficient was the opposite to that of the radial coefficient. As differential stress was increased, the axial

Skempton coefficient decreased. When differential stress decreased, the axial Skempton coefficient increased back to its starting value of around 0.2. At the maximum differential stress of 400 MPa, the axial Skempton coefficient was at its minimum of around -0.15. Therefore, an increase in axial stress of 5 MPa caused pore pressure to decrease by around 0.25 MPa (Figures 8a and 8e). The axial Skempton coefficient was also negative at a differential stress of 310 MPa, and at a differential stress of 220 MPa following the stress increases to both 310 MPa (cycle 2) and 420 MPa (cycle 3).

We also calculated the errors (standard deviation) of the averaged B_x and B_z values (Table 1). The errors in the averaged radial Skempton coefficients are much larger (up to 0.186) than in the average axial Skempton coefficients (up to 0.029).

3.5. Estimated Apparent Skempton Coefficients From Ultrasonic Data

The Skempton coefficients were also calculated indirectly from the ultrasonic wave velocity measurements at the same positions as the direct measurements during cycles 0 to 3. We determined the Skempton coefficients, using Equations 7 and 8, from the drained elastic compliances (S_{ijkl}), which were calculated from the unrelaxed elastic moduli using the crack density tensors. The final results are shown in Figure 13, and crack densities and fitted velocity variations are shown in Figures 11 and 12, respectively.

The inverted crack densities show a dominant contribution of α_{11} and β_{1111} , which reflect the apparent evolution of anisotropy in wave velocity. The crack density component α_{33} , β_{1133} and β_{3333} were substantially lower than α_{11} and β_{1111} , and decreased with increasing differential stress. Repeating the inversion procedure without the zero lower bound constraint on crack density components would produce slightly negative values of α_{33} and β_{3333} , and slightly better fit to data, which points to either an inadequacy of the effective medium theory employed, or, more likely, to a bias in the absolute values of the P and Sh wave velocities measured by manual picks of the reference survey. Despite this limitation, the overall fit to data is acceptable (Figure 12) and well within the picking errors. The relative evolution of both α_{11} and β_{1111} show an increase with increasing differential stress during cycles 2 and 3, and a stable behavior during cycle 1.

The resulting inferred radial Skempton coefficient (B_x) increased with increasing differential stress (Figure 13, circles). Initially, prior to load cycles at 20 MPa differential stress, B_x was 0.45 and increased to 0.85 at 400 MPa differential stress (the maximum of cycles). There was a small amount of hysteresis at low differential stress, B_x increased by around 0.05 units following each stress cycle.

The computed axial Skempton coefficient (B_z) was small, of the order of 0.05, and systematically negative. It slightly decreased with increasing differential stress (Figure 13, triangles). Initially, at 20 MPa differential stress,

ELSIGOOD ET AL.

21699356, 2025, 11, Downloaded from https://agupubs.onlinelibrary.wiley.com/doi/10.1029/2025JB032593 by Nicolas Brantut - Helmholtz-Zentrum Potsdam GFZ, Wiley Online Library on [05/11/2025]. See the Terms and Conditions

conditions) on Wiley Online Library for rules of use; OA articles are governed by the applicable C

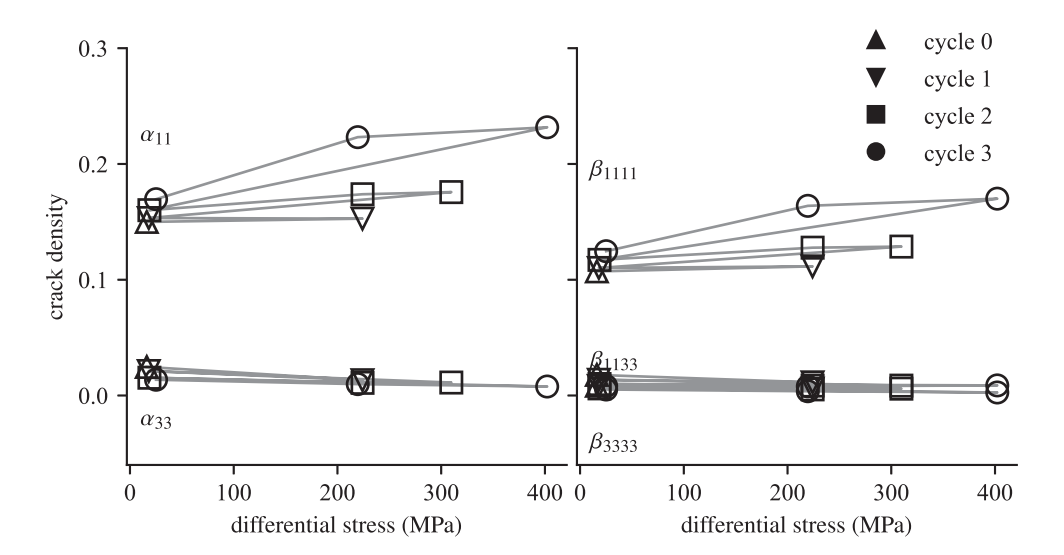


Figure 11. Crack densities inverted using Equation 3 from the high-frequency unrelaxed elastic moduli by assuming that the Young's modulus of the solid matrix (E_0) was 89 GPa, the Poisson's ratio (ν_0) was 0.22, the bulk modulus of the fluid $(K_{\rm fl})$ was 2.2 GPa, and the crack aspect ratio (ζ) was 10^{-3} . These crack densities were used to calculate the drained compliances leading to the estimated Skempton coefficients in Figure 13.

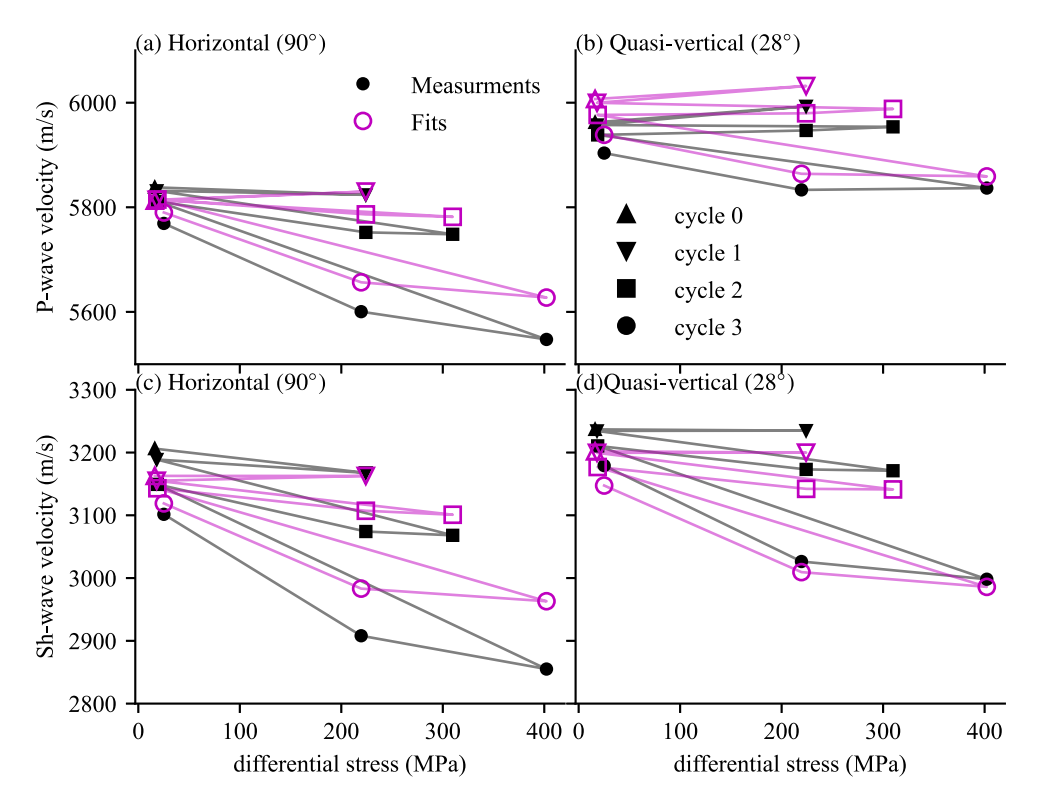


Figure 12. Measured group velocities (solid black symbols) and fits (open magenta symbols) during differential stress cycles. We measured P-wave velocities across paths at five different angles relative to the (vertical) direction of compression and Shwave velocities at three different angles. Here we show the velocities measured at the two most extreme angles to the vertical: (a) P-wave velocity measured horizontally; (b) P-wave velocity measured at 28° (quasi-vertical); (c) Sh-wave velocity measured horizontally; and (d) Sh-wave velocity measured at 28°.

ELSIGOOD ET AL. 14 of 23

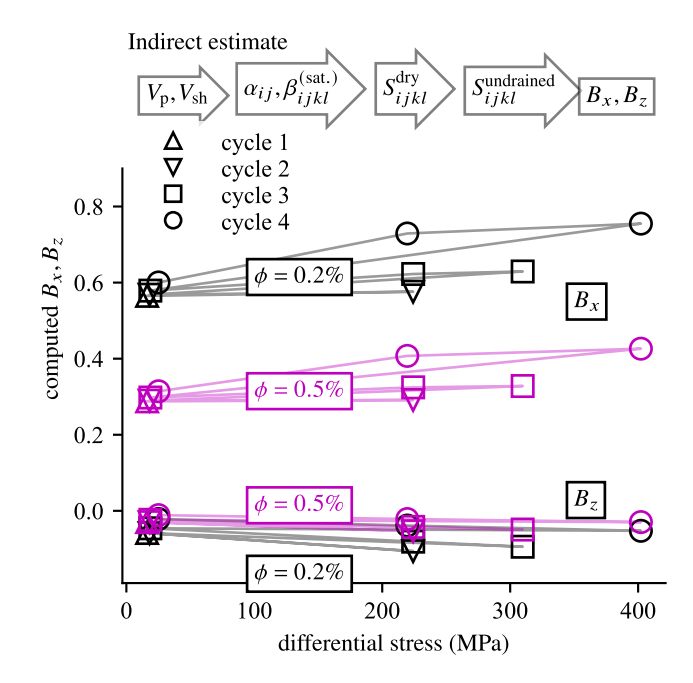


Figure 13. The axial and radial Skempton coefficients calculated using Equations 7 and 8 from the drained compliance matrix, which were calculated indirectly. The ultrasonic wave velocities were used to calculate in-turn the unrelaxed compliances, crack densities, drained compliances, and then the Skempton coefficients assuming that the Young's modulus of the solid matrix (E_0) was 89 GPa, the Poisson's ratio (ν_0) was 0.22, the bulk modulus of the fluid $(K_{\rm fl})$ was 2.2 GPa, and the porosity (ϕ) was either 0.5% (magenta) or 0.2% (black).

Bz was -0.03 and decreased to -0.06 at the maximum differential stress at 400 MPa. There was hysteresis at low differential stress, with B_z being around 0.05 smaller following all stress cycles.

The estimates of the radial Skempton coefficient were systematically lower than the directly measured values by around 0.2. Despite this quantitative difference, the qualitative sense of evolution during the large amplitude stress cycles was similar.

4. Discussion

4.1. Qualitative Behavior of the Apparent Skempton Coefficients

We observed general trends of decreasing axial apparent Skempton coefficient B_z and increasing radial apparent Skempton coefficient B_x with increasing differential stress. These trends were similar for both directly measured values (Figure 10) and for values estimated from ultrasonic wave velocities (Figure 13). The trends in B_x and B_z are consistent with previous measurements in Berea sandstone (Lockner & Stanchits, 2002) and our measurements on thermally cracked Westerly granite samples (Elsigood et al., 2023).

The observed behavior corresponds to a stress-induced anisotropic response, where the Skempton coefficients become increasingly anisotropic with the application of increased differential stress. As indicated by our measurements of P-wave and Sh-wave velocities in the horizontal and sub-vertical directions, and consistently with previously published results in similar materials and conditions (e.g., Paterson & Wong, 2005, Section 5.4.3), the initial increase in axial stress predominantly closes pre-existing microcracks aligned perpendicular to the axis of compression, with further increases in axial stress causing the generation of new tensile microcrack damage with cracks aligned parallel to the direction of compression. This anisotropic crack orientation

distribution leads to differences in the radial and axial compliances and that in turn leads to the anisotropy in the Skempton coefficients.

Westerly granite is often considered to have minimal pre-existing anisotropy, and therefore we would only expect minimal differences between B_x and B_z prior to deformation. However, it is likely that intrinsic elastic anisotropy exists even at high confining pressure (Lokajíček et al., 2021). Additionally, the larger than expected differences could be the result of uncertainties in our measurements, which will now be addressed.

4.2. Uncertainties and Limitations of Direct Measurements

The variation in the repeated measurements of B_x and B_z is quantified using the standard deviation. The standard deviation of measurements of B_x is much larger than for B_z . Therefore, relative differences between values of B_x calculated at different stress levels should be considered within the context of these larger errors. In the worst case, for B_x during cycle 3 at 26 MPa differential stress, the mean is 0.59 and standard deviation is 0.186 and therefore 95% of values would be expected to lie in the range of 0.23–0.95. In the best case, for B_x during cycle 1 at 18 MPa differential stress, the mean is 0.69 and standard deviation is 0.036 and therefore 95% of values would be expected to lie in the range of 0.62–0.76. For all values of B_z , the standard deviation is lower than the lowest value for B_x , and considerably so for most.

One source of the larger variance in the B_x values compared with the B_z values is the repeatability of the stress steps themselves. Axial stress steps were conducted using a servo-controlled constant rate (ramp) change, which was reproducible for both increases and decreases. By contrast, confining pressure was changed in steps using a hand-pump and decreased by releasing a valve, so these changes were not as reproducible (see Appendix A for assumptions on confining pressure changes resulting in only radial stress steps).

Along with the variation within repeat measurements, we must also consider a bias within the measured pore pressure changes. In low diffusivity rocks, the pore pressure transducers have a delay in measuring the pore

ELSIGOOD ET AL. 15 of 23

pressure changes due to the time taken for pore pressure to equilibrate between the low-volume transducers and the local pore volume of the sample (see Figure 4). The delay time will be small for confining pressure changes because the confining pressure acts on the fluid in the sensor simultaneously with the fluid in the rock pore space. Therefore, measurements of B_z will likely have been underestimated and the actual B_z will have been higher when positive and lower when negative.

At the highest loads, time-dependent variations in radial strain were detected, superimposed on variations linked to stress steps. These time-dependent changes indicate the occurrence of inelastic processes, such as brittle creep (Brantut et al., 2013) or dilatancy recovery (Brantut & Petit, 2023; Holcomb, 1981; Scholz & Kranz, 1974). The potential for brittle creep was limited by the fact that load was reduced from its peak. Typical strain rates for the time-dependent changes observed here were of the order of 10^{-9} to 10^{-8} s⁻¹, and no long-term trend was observed in terms of pore pressure changes. Therefore, we consider that the long-term inelastic changes did not significantly impact the measurements conducted in response to stress steps. This is supported by the repeatability and reversibility of the pore pressure response to stress steps.

Since the pore pressure variations were measured locally, there is also a potential bias that could be due to sample heterogeneity. As illustrated in Figure 4 and verified throughout our data set, all pore pressure transducers responded consistently in the same sense of variation in response to stress steps. The only differences were in amplitude (as anticipated from theory, see Figure 3) and in delay time. The variations in delay time are likely due to variations in local hydraulic diffusivity, as well as the quality of coupling between the sensor stem and rock that could modify fluid flow at the interface. Such delays only indicate possible variations in transport properties, but do not imply large differences (and certainly not differences in sign) in the amplitude of the undrained pore pressure response. The lack of substantial sample heterogeneity is further supported by the excellent agreement between our local strain gauge data.

4.3. Comparison Between Direct and Indirect Estimates of Apparent Skemption Coefficients

The ultrasonic wave velocities are calculated using a cross-correlation method, compared with a reference survey where arrival times are manually picked. The absolute arrival times of Sh-waves, in particular, are difficult to determine due to interactions with the arrival of the faster P-waves. Changes in wave velocity using the cross-correlation method introduces minimal errors. However, absolute values of wave velocity are required to invert for the unrelaxed elastic compliance matrix. Therefore, absolute errors introduced from the manual picks become important.

Effective medium theory was used to calculate the drained elastic compliance matrix from the unrelaxed compliance matrix via the crack density tensors. To invert for the crack density tensor, we have to make an assumption of the elastic moduli of the intact material: $E_0 = 89$ GPa and $\nu_0 = 0.22$. These cannot be known exactly, but they influence the crack densities and therefore also the calculated drained elastic compliance matrix. We also estimated the axial and radial Skempton coefficients using Equations 7 and 8, which again required values of E_0 and ν_0 . Additionally, the calculated values of B_x and B_z have a strong dependence on the estimate of porosity, illustrated by the significant differences between the Skempton coefficients calculated using a porosity of 0.2% (Figure 13, black points) and 0.5% (Figure 13, magenta points). Therefore, the exact values of the estimated B_x and B_z should be considered indicative.

While the values of B_x and B_z estimated from ultrasonic wave velocities follows the same qualitative trend as that directly measured with pore pressure variations, quantitative discrepancies suggest a systematic bias. Beyond the aforementioned sources of error, it is likely that the dominant problem is the fundamental difference between static moduli (measured, say, using load-unload cycles of around 1 MPa amplitude) and dynamic moduli (where the associated stress changes are orders of magnitude smaller). Even in dry, low porosity materials, it is well documented that static and dynamic moduli differ, sometimes by up to a factor of two at low pressure, and that this difference decreases with increasing pressure (e.g., C. H. Cheng & Johnston, 1981). In Westerly granite at 40 MPa effective confining pressure, we expect a discrepancy of the order of 25% (C. H. Cheng & Johnston, 1981; Martin & Chandler, 1994), which will translate into large errors in Skemption coefficients. Thus, our estimates (Figure 13) are only qualitative, but they correctly capture the trend with changing conditions. These results are consistent with previous data on thermally cracked Westerly granite (Elsigood et al., 2023), which showed a

ELSIGOOD ET AL. 16 of 23

substantial quantitative discrepancy between measured and predicted Skempton coefficient at low effective pressure, and a comparatively smaller error at more elevated pressure.

4.4. Hysteresis of Apparent Undrained Poroelastic Coefficients

There is minimal hysteresis in the axial Skempton coefficient at 20 MPa differential stress comparing measurements at cycle 0 with cycles 1, 2, and 3 (Figure 10). However, there is a noticeable trend in the axial Skempton coefficient at around 200 MPa differential stress which is decreasing when measured after each cycle, where B_x at cycle 3 is lower than at cycle 2, which is itself lower than at cycle 1 (Figure 10). The microstructural changes induced by the large amplitude (greater than 100 MPa) differential loading cycles, first closing cracks perpendicular to the direction of compression, and then opening cracks parallel to the compressional axis, dictate the value of the axial Skempton coefficient. Therefore, the reversibility of the microstructural changes dictates the hysteresis of the poroelastic response. Tensile cracks that were created at high stress, above 220 MPa, are not expected to close again straight away when stress is decreased to 220 MPa due to only partial back sliding of cracks (e.g., David & Zimmerman, 2011). It is not until stress is decreased much further that we see B_z return to positive values.

There was noticeable hysteresis in the undrained Young's modulus (E_z^u) at around 20 MPa differential stress between cycles 0 and 3. However, we are not able to interpret any hysteresis during intermediate cycles 1 and 2 due to the larger variation in measurements (Table 1). This hysteresis is likely due to the damage caused at high stress, permanently reducing the stiffness.

There was no noticeable hysteresis in the Skempton coefficients in the small rapid undrained unloading and loading cycles, which is consistent with prior measurements by (Elsigood et al., 2023; Lockner & Stanchits, 2002).

The hysteresis in apparent Skempton coefficients during the large amplitude cycles parallels the hysteresis in stress-strain behavior (Figure 6). While only minimal hysteresis in axial and volumetric strain was observed during cycle 1, large hysteresis loops occurred during cycles 2 and 3. In particular, the volumetric strain experienced a limited change upon unloading between 340 and 220 MPa, of the order of that expected from the elastic contribution; the inelastic change was thus nearly unchanged. Remarkably, both apparent Skempton's coefficients remained also nearly unchanged between those two stresses. Similarly, limited recovery of apparent Skempton's coefficients was observed during unloading from 400 to 220 MPa in cycle 3. In that same interval, volumetric strain was nearly constant. Overall, the apparent Skempton's coefficients appear to be strongly correlated to the (inelastic) volumetric strain.

4.5. A Negative Pore Pressure Response

At high differential stress we measured a decreasing pore pressure response to increases in axial stress (negative B_z). This effect was measured at four of the nine positions of differential stress in the overall stress cycles: at 307 MPa and then at 223 MPa during cycle 2, and at 404 MPa and then at 222 MPa during cycle 3 (Table 1).

The apparent axial Skempton's coefficient measured at each of the nine stress positions were reproducible for increases and decreases in axial stress (Figures 7 and 8) and the variation between measurements was small (Table 1, B_z : SD). In particular, the measurements of negative B_z were consistent in causing both decreases in pore pressure from increases in differential stress and increases in pore pressure from decreases in axial stress.

Even when the apparent axial Skempton coefficient was negative, the apparent bulk Skempton coefficient $(B = (2/3)B_x + (1/3)B_z)$ was always positive, due to the contribution of the much higher apparent radial Skempton coefficient. Therefore, hydrostatic compression of the sample would not result in a decrease in pore pressure.

4.5.1. Comparison With Previous Data Sets

To our knowledge, negative values of (apparent) Skempton's coefficients in the direction of loading have not been reported previously in the literature. Our data can be compared to those of Lockner and Stanchits (2002), who explored the pore pressure changes due to change in mean stress and deviatoric stress with increasing overall differential stress in Berea sandstone, Navajo sandstone, packed Ottawa sand, and a porous aluminum oxide

ELSIGOOD ET AL. 17 of 23

ceramic. Lockner and Stanchits (2002) reported their results in terms of coefficients B and η related to the axial (B_z) and radial (B_x) Skempton coefficients by

$$B_x = B - \frac{3}{4}\eta,\tag{9a}$$

and

$$B_z = B + \frac{3}{2}\eta. \tag{9b}$$

The results of Lockner and Stanchits (2002) show that, for Berea sandstone, Navajo sandstone, and Ottawa sand pack, B is approximately constant with increasing differential stress, and η becomes increasingly negative with increasing differential stress. This equates to an increasing B_x and decreasing B_z with increasing differential stress, consistent with the trends we find here. Lockner and Stanchits (2002) found no pore pressure response from changes in deviatoric stress ($\eta=0$) in the porous ceramic for increasing differential stress. Using Equation 9b, B_z is negative when $B<-(3/2)\eta$. In Berea sandstone, at the highest deviatoric stress shown of 55 MPa (approximately 80% of the failure stress), B ranged from 0.49 to 0.54, and η ranged from -0.36 to -0.30 (Lockner & Stanchits, 2002). Therefore, B_z was in the range of -0.05 to +0.09 and we can infer that at high stress in Berea sandstone it is possible to have a negative pore pressure response to increases in axial stress. However, their data at 80% of failure stress were the least reproducible of their results.

In a follow-up work, Lockner and Beeler (2003) report exclusively nonnegative values of B_z in Berea sandstone, but the decreasing trend of B_z with increasing load remained. The same trend was observed in thermally cracked Westerly granite tested at low overall differential stress (below the dilatancy threshold) in Elsigood et al. (2023).

Therefore, it appears that negative B_z can only be observed in tight, cracked rock under elevated differential stresses, beyond the onset of dilatancy. In our tests on granite, negative B_z are observed when the rock has been brought to stresses beyond the onset of net dilation (around 300 MPa, 58% of the failure stress). This threshold might not have been reached in the tests conducted on porous sandstone by Lockner and Stanchits (2002) and Lockner and Beeler (2003), possibly due to the large existing porosity that could mask, at least in part, the dilatant effects of microcracks. As a test of this idea, we consider the behavior of the porous ceramic sample in Lockner and Stanchits (2002), which is used as a control where the pore space is dominated by equant pores with few low-aspect ratio microcracks. The porous ceramic does not show any deviatoric stress dependence ($\eta = 0$), but it still shows some pore pressure response to mean stress with B = 0.12 to 0.13 even at high deviatoric stress. This type of equant pore will still exist in Berea sandstone even at high differential stress, helping to offset some of the negative pore pressure response to changing axial stress. By contrast, in Westerly granite, there are essentially no equant pores to offset the negative pore pressure effects of opening cracks.

4.5.2. Micromechanics of a Negative Axial Skempton Coefficient

We now consider what a negative axial Skempton coefficient (B_z) means in terms of the micromechanical model of A. H.-D. Cheng (1997). In Equation 8, the denominator is always positive (as porosity, ϕ , is negligible and the bulk modulus of the sample will be smaller than the bulk modulus of the solid constituents) so we consider only the numerator: $3(2S_{13} + S_{33}) - 1/K_0$. We express the numerator in terms of the drained Young's modulus and Poisson's ratio as $3(1 - 2\nu_z)/E_z - 3(1 - 2\nu_0)/E_0$, so that

$$B_z < 0$$
 if $\frac{1 - 2\nu_z}{1 - 2\nu_0} < \frac{E_0}{E_z}$. (10)

In rocks subject to triaxial stress states with mostly closed horizontal cracks and a population of open subaxial microcracks, we anticipate that E_z should be close to E_0 , so the numerator becomes close to $E_0 = \frac{E_0}{E_0}$. Therefore, $E_0 = \frac{E_0}{E_0}$ is negative when the Poisson's ratio of the sample is greater than the Poisson's ratio of the solid matrix:

$$B_z < 0$$
 if $\nu_z \gtrsim \nu_0$, (11)

ELSIGOOD ET AL. 18 of 23

assuming that the Young's modulus of the material is approximately equal to the Young's modulus of the solid matrix $(E_z \approx E_0)$.

In tight rocks, the situation $\nu_z > \nu_0$ is commonly observed during inelastic deformation (e.g., Faulkner et al., 2006; Walsh, 1965a) and can be interpreted as nonlinear buckling of the loading-bearing solid between cracks (Ashby & Hallam, 1986), slip at microscale interfaces (e.g., David et al., 2012, 2020; Walsh, 1965a) and/or slip-induced opening of tensile microcracks (e.g., M. L. Kachanov, 1982; Basista & Gross, 1998). However, conventional models that include microscale slip possibly coupled to tensile crack opening usually predict perfect linear elastic behavior at the onset of unloading due to nonzero friction that prevents immediate backslip, and thus no change in Poisson's ratio and significant crack closing/opening (e.g., Walsh, 1965a). Such model predictions are consistent with the existence of a "deadband" in variations of wave velocities and dilatancy at the onset of unloading; such a deadband is not always observed (Stevens & Holcomb, 1980), even though there is indeed strong hysteresis in properties during unloading (e.g., Brantut & Petit, 2023; Passelègue et al., 2018; Zoback & Byerlee, 1975b). The reversibility we observe in terms of pore pressure change during rapid, small amplitude load-unload cycles is thus the manifestation of either (a) direct crack opening/closure not linked to frictional effects (e.g., nonlinear buckling effects such as those described by Ashby and Hallam (1986)), or (b) slip at near frictionless shear cracks within the material.

To further examine the conditions under which negative B_z may appear in cracked rocks, we can use the anisotropic crack model of Sayers and Kachanov (1995) (Equation 3) with A. H.-D. Cheng (1997)'s expression (8), which leads to (Wong, 2017):

$$B_z = \frac{3h(\alpha_{33} + \psi(\beta_{3333} + 2\beta_{1133}))}{2S_{11} + 2S_{12} + 4S_{13} + S_{33} + \phi/K_{fl} - (1 + \phi)/K_0},$$
(12)

where $\psi = -\nu_0/2$ (dry limit), so that

$$B_z < 0$$
 is equivalent to $\alpha_{33} - \frac{\nu_0}{2} (\beta_{3333} + 2\beta_{1133}) < 0.$ (13)

From relationships between crack density tensors α_{ii} and β_{iikl} (Guéguen & Sarout, 2009), we have

$$\alpha_{33} = \beta_{3333} + 2\beta_{1133},\tag{14}$$

which makes condition (Equation 13) impossible to satisfy rigorously. In our indirect estimates of B_z from ultrasonic data, we did not enforce the equality (Equation 14); we obtained slightly negative B_z , which is inconsistent with the underlying model assumptions. Since all the inferred α_{33} , β_{1133} and β_{3333} were close to zero, the indirect estimates only indicate that B_z is also close to zero (which is consistent with the direct estimates), but that combined measurement errors and model limitations are too large to properly constrain the eventual sign of B_z .

The impossibility of obtaining negative B_z from the model of Wong (2017) originates from the assumption that open cracks do not open further, close or slide in the computation of effective compliances. It reinforces the idea that negative B_z likely arises from either nonlinear effects (crack opening/closing) or microscale slip effects (which are invisible to ultrasonic data and not modeled in Sayers and Kachanov (1995)). Nonlinearity could come from variations in crack density tensors in response to applied stress (e.g., Holcomb, 1981). Our wave velocity data showed no resolvable change during each stress step, even at the highest tested applied load, which indicates a limited nonlinearity in terms of crack density. It is possible that more accurate measurements could detect crack density variations during stress steps, so we cannot completely rule out this process.

Thus, it appears that the negative apparent axial Skempton coefficient must be the result of nonlinear processes. It is thus likely that the apparent B_z we measured are stress-sensitive, that is, the value must depend on the amplitude of the perturbation. We used stress steps of a few MPa, which resulted in a few 10 s of microstrain. Exploring the effect of the amplitude of the perturbation would be an attractive experimental approach to better constrain the micromechanical origin of negative (resp. positive) pore pressure changes in response to increasing (resp. decreasing) axial stress steps.

ELSIGOOD ET AL. 19 of 23

4.6. Implications

Undrained poroelastic properties of rocks are key quantities that impact stress and deformation in the Earth's brittle crust. Specifically, the Skempton coefficient enters in descriptions of short-term stress transfer around fault zones following earthquakes (e.g., Jónsson et al., 2003; Peltzer et al., 1998).

In their early work, Cocco and Rice (2002) suggested that fault damage zones might be adequately modeled by an anisotropic material with a Skempton coefficient that is near zero in all directions except perpendicular to the fault plane, that is, only fault-normal changes in stress lead to substantial (undrained) changes in pore pressure. This assumption is consistent with the existence of microcracks parallel to the fault plane (Wong, 2017). Our new data on cracked granite are in full support of this hypothesis: in our experiment, the dominance of axial microcracks leads to high (positive) values of the radial Skempton coefficient, and small (negative) values of the axial Skempton coefficient.

The fact that the Skempton coefficient in the axial direction can be negative has large implications for stress redistribution around faults after earthquakes. In which situation will this effect be significant? It is worth noting that negative axial Skempton coefficients are only observed beyond the onset of dilation, that is, at a stress state that is commensurate with the frictional strength of the faulted rock (e.g., Hadley, 1975, Chapter 1). Thus, we expect that only the regions that experienced high stress prior to an earthquake will have a negative Skempton coefficient in the direction of the largest principal stress. In practice, the stress state in the crust is generally considered to be close to the frictional strength of faults (Brudy et al., 1997; Zoback & Healy, 1992), so that the material around optimally oriented faults is not stressed enough to have a negative Skempton coefficient. Thus, regions where Skempton can be negative are likely to be around misoriented faults (or branches) and geometrical irregularities such as transpressive relays. Systematic investigations are required to determine precisely the extent and conditions where a substantially negative Skempton effect can be observed in nature.

5. Conclusions

During deformation of Westerly granite at elevated pressure and ambient temperature, the axial and radial Skempton coefficients become progressively anisotropic with increasing differential stress: the axial Skempton coefficient B_z decreases, and the radial Skempton coefficient B_x increases with increasing load. The stress-induced anisotropy mostly recovers when differential stress is removed. There is hysteresis between the loading and unloading curves; where the anisotropy is not recovered after an initial reduction in differential stress. This is comparable to similar hysteresis in pore volume, elastic wave velocities and permeability in cyclic loading tests performed on Westerly granite (Brantut & Petit, 2023; Holcomb, 1981; Mitchell & Faulkner, 2008; Passelègue et al., 2018; Zoback & Byerlee, 1975a, 1975b) and is likely due to the difference between the onset of sliding on shear cracks when loading and the onset of backsliding when unloading.

The apparent axial Skempton coefficient B_z becomes negative at high stress, that is, an increase in axial stress caused a decrease in pore pressure. The negative pore pressure effect was repeatable for unloading and reloading of the sample, and is correlated to the existence of subaxial dilatant microcracks that dominate the volumetric strain response of the rock. Dilatancy under compression is considered a non-linear process caused by sliding on shear cracks leading to the opening of tensile cracks. However, the reversibility of the process from unloading and reloading of small axial stress suggests that the initial microstructural changes causing dilatancy are approximately linear.

Attempts to make predictions of Skempton's coefficients from dynamic elastic wave velocity data produce poor quantitative agreement, even when the data are suitably corrected for frequency effects. This discrepancy is likely due to accumulated errors in the inference of dynamic moduli and crack density tensors from possibly inaccurate velocity data. However, the sense of variation and orders of magnitudes of B_x and B_z are still correctly captured by the predictions.

Appendix A: Radial Stress Changes

Under undrained conditions, pore pressure changes with stress due to the Skempton effect are given by

ELSIGOOD ET AL. 20 of 23

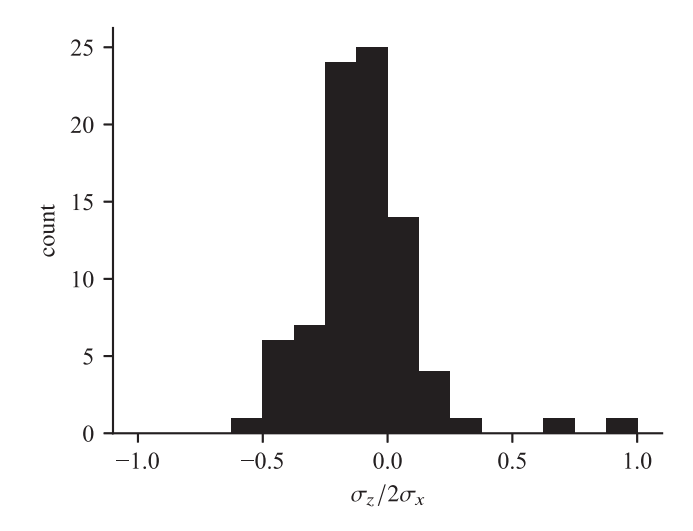


Figure A1. A histogram of half the ratio of the axial stress change with confining pressure change. When multiplied by the axial Skempton coefficients this is the correction needed to our radial Skempton coefficients when considering that confining pressure steps are not purely radial (Equation A2).

$$\Delta p = \frac{2}{3} \Delta \sigma_x B_x + \frac{1}{3} \Delta \sigma_z B_z, \tag{A1}$$

where Δp is the change in pore pressure, $\Delta \sigma_x$ and $\Delta \sigma_z$ are the changes in radial and axial stress, respectively, and B_x and B_z are the radial and axial Skempton coefficients, respectively. By assuming confining pressure changes produce only changes in radial stress, B_x was calculated as $3\Delta p/2\Delta\sigma_x$, but if this assumption cannot be made then we must correct B_x for axial stress changes, according to

$$B_x = \frac{3}{2} \frac{\Delta p}{\Delta \sigma_x} - \frac{\Delta \sigma_z}{2\Delta \sigma_x} B_z. \tag{A2}$$

The magnitude of the correction factor is small because both $\Delta \sigma_z/2\Delta\sigma_x$ and B_z are small. The axial stress change with confining pressure $(\Delta\sigma_z/2\Delta\sigma_x)$ is mostly between -0.25 and 0.25 (Figure A1) and B_z was between -0.2 and 0.2. Therefore we would expect the correction to B_x to be within 0.04. Indeed, if we corrected our calculated B_x values, the worst case change would be less than 0.03, and in most cases it would be less than 0.01. Given the large errors shown in B_x (Table 1), incorporating these correction factors would not significantly effect the main results.

Conflict of Interest

The authors declare no conflicts of interest relevant to this study.

Data Availability Statement

Data are available at Elsigood et al. (2024).

Acknowledgments R

We acknowledge financial support from the UK Natural Environment Research Council through Grants #NE/L002485/1 to B.E., #NE/S000852/1 to N.B. and #NE/T007826/1 to T.M. and P.M., the European Research Council under the European Union's Horizon 2020 research and innovation programme (projects RockDeaf, grant agreement #804685, and RockDeath, grant agreement #101088963, to N.B.) and the Leverhulme Trust through a Philip Leverhulme Prize to N.B. Critical review comments by Teng-Fong Wong and Lucas Pimienta helped clarify many points of the manuscript.

References

Aben, F. M., Brantut, N., Mitchell, T. M., & David, E. C. (2018). Rupture energetics and changing elastic properties in crustal rock from laboratory-scale seismic tomography. In (Abstract T13B-08 presented at 2018 Fall Meeting, AGU, Washington DC, 10-14 Dec.).

Ashby, M. F., & Hallam, S. D. (1986). The failure of brittle solids containing small cracks under compressive stress states. *Acta Metallurgica*, 34(3), 497–510.

Basista, M., & Gross, D. (1998). The sliding crack model of brittle deformation: An internal variable approach. *International Journal of Solids and Structures*, 35(5–6), 487–509. https://doi.org/10.1016/s0020-7683(97)00031-0

Benson, P. M., Meredith, P. G., Platzman, E. S., & White, R. E. (2005). Pore fabric shape anisotropy in porous sandstones and its relation to elastic wave velocity and permeability anisotropy under hydrostatic pressure. *International Journal of Rock Mechanics and Mining Sciences*, 42(7–8), 890–899. https://doi.org/10.1016/j.ijrmms.2005.05.003

Brace, W. F., & Martin, R. J. (1968). A test of the law of effective stress for crystalline rocks of low porosity. *International Journal of Rock Mechanics and Mining Sciences*, 5, 415–426. https://doi.org/10.1016/0148-9062(68)90045-4

Brace, W. F., Paulding, B. W., Jr., & Scholz, C. (1966). Dilatancy in the fracture of crystalline rocks. *Journal of Geophysical Research*, 71(16), 3939–3953. https://doi.org/10.1029/jz071i016p03939

Brantut, N. (2015). Time-dependent recovery of microcrack damage and seismic wave speeds in deformed limestone. *Journal of Geophysical Research*, 120(12), 8088–8109. https://doi.org/10.1002/2015JB012324

Brantut, N. (2020). Dilatancy-induced fluid pressure drop during dynamic rupture: Direct experimental evidence and consequences for earthquake dynamics. Earth and Planetary Science Letters, 538, 116179. https://doi.org/10.1016/j.epsl.2020.116179

Brantut, N., & Aben, F. M. (2021). Fluid pressure heterogeneity during fluid flow in rocks: New laboratory measurement device and method. Geophysical Journal International, 225(2), 968–983. https://doi.org/10.1093/gji/ggab019

Brantut, N., Heap, M. J., Meredith, P. G., & Baud, P. (2013). Time-dependent cracking and brittle creep in crustal rocks: A review. *Journal of Structural Geology*, 52, 17–43. https://doi.org/10.1016/j.jsg.2013.03.007

Brantut, N., & Petit, L. (2023). Micromechanics of rock damage and its recovery in cyclic loading conditions. *Geophysical Journal International*, 233(1), 145–161. https://doi.org/10.1093/gji/ggac447

Brudy, M., Zoback, M. D., Fuchs, K., Rummel, F., & Baumgärnter, J. (1997). Estimation of the complete stress tensor to 8 km depth in the KTB scientific drill holes: Implications for crustal strength. *Journal of Geophysical Research*, 102(B8), 18453–18475. https://doi.org/10.1029/96ib02942

Carslaw, H. S., & Jaeger, J. C. (1959). Conduction of heat in solids (2nd ed.). Oxford University Press.

Cheng, A. H.-D. (1997). Material coefficients of anisotropic poroelasticity. *International Journal of Rock Mechanics and Mining Sciences*, 34(2), 199–205. https://doi.org/10.1016/s0148-9062(96)00055-1

ELSIGOOD ET AL. 21 of 23

- Cheng, C. H., & Johnston, D. H. (1981). Dynamic and static moduli. Geophysical Research Letters, 8(1), 39–42. https://doi.org/10.1029/g1008i001p00039
- Cocco, M., & Rice, J. R. (2002). Pore pressure and poroelasticity effects in Coulomb stress analysis of earthquake interactions. *Journal of Geophysical Research*, 107(B2). https://doi.org/10.1029/2000JB000138
- David, E. C., Brantut, N., & Hirth, G. (2020). Sliding crack model for nonlinearity and hysteresis in the triaxial stress-strain curve of rock, and application to antigorite deformation. *Journal of Geophysical Research*, 125(10), e2019JB018970. https://doi.org/10.1029/2019JB018970
- David, E. C., Brantut, N., Schubnel, A., & Zimmerman, R. W. (2012). Sliding crack model for nonlinearity and hysteresis in the uniaxial stress-strain curve of rock. *International Journal of Rock Mechanics and Mining Sciences*, 52, 9–17. https://doi.org/10.1016/j.ijrmms.2012.02.001
- David, E. C., & Zimmerman, R. W. (2011). Compressibility and shear compliance of spheroidal pores: Exact derivation via the Eshelby tensor, and asymptotic expressions in limiting cases. *International Journal of Solids and Structures*, 48(5), 680–686. https://doi.org/10.1016/j.ijsolstr. 2010.11.001
- Eccles, D., Sammonds, P. R., & Clint, O. C. (2005). Laboratory studies of electrical potential during rock fracture. *International Journal of Rock Mechanics and Mining Sciences*, 42(7–8), 933–949. https://doi.org/10.1016/j.ijrmms.2005.05.018
- Elsigood, B., Brantut, N., Meredith, P. G., Healy, D., Mitchell, T. M., & Aben, F. M. (2023). Stress induced anisotropic poroelasticity in Westerly granite. *Journal of Geophysical Research*, 128(11), e2023JB026909. https://doi.org/10.1029/2023JB026909
- Elsigood, B., Brantut, N., Meredith, P. G., & Mitchell, T. M. (2024). The poroelastic response of westerly granite subjected to cyclical changes in load: Mechanical and ultrasonic data [Dataset]. Zenodo. https://doi.org/10.5281/zenodo.12113742
- Faulkner, D. R., Mitchell, T. M., Healy, D., & Heap, M. J. (2006). Slip on 'weak' faults by the rotation of regional stress in the fracture damage zone. *Nature*. 444(7121), 922–925. https://doi.org/10.1038/nature05353
- Ghabezloo, S., & Sulem, J. (2010). Effect of the volume of the drainage system on the measurement of undrained thermo-poro-elastic parameters. International Journal of Rock Mechanics and Mining Sciences, 47(1), 60–68, https://doi.org/10.1016/j.jirmms.2009.03.001
- Guéguen, Y., & Kachanov, M. (2011). Effective elastic properties of cracked and porous rocks An overview. In Y. M. Leroy & F. K. Lehner (Eds.), *Mechanics of crustal rocks* (pp. 73–125). Springer.
- Guéguen, Y., & Sarout, J. (2009). Crack-induced anisotropy in crustal rocks: Predicted dry and fluid-saturated Thomsen's parameters. Physics of the Earth and Planetary Interiors, 172(1–2), 116–124. https://doi.org/10.1016/j.pepi.2008.05.020
- Hadley, K. (1975). Dilatancy: Further studies in crystalline rock. (Ph. D. Thesis). Massachusetts Institute of Technology.
- Hart, D. J., & Wang, H. F. (2001). A single test method for determination of poroelastic constants and flow parameters in rocks with low hydraulic conductivities. *International Journal of Rock Mechanics and Mining Sciences*, 38(4), 577–583. https://doi.org/10.1016/s1365-1609(01) 00023-5
- Holcomb, D. J. (1981). Memory, relaxation, and microfracturing in dilatant rock. *Journal of Geophysical Research*, 86(B7), 6235–6248. https://doi.org/10.1029/jb086jb07p06235
- Jaeger, J. C., Cook, N. G. W., & Zimmerman, R. W. (2007). Fundamentals of rock mechanics (4th ed.). Blackwell Publishing.
- Jónsson, S., Segall, P., Pederson, R., & Björnsson, G. (2003). Post-earthquake ground movements correlated to pore-pressure transients. *Nature*, 424(6945), 179–183. https://doi.org/10.1038/nature01776
- Kachanov, M. (1993). Elastic solids with many cracks and related problems. In J. W. Hutchinson & T. Y. Wu (Eds.), Advances in applied mechanics (Vol. 30, pp. 259–445). Academic Press. https://doi.org/10.1016/S0065-2156(08)70176-5
- Kachanov, M. L. (1982). A microcrack model of rock inelasticity. Part II: Propagation of microcracks. Mechanics of Materials, 1, 29–41. https://doi.org/10.1016/0167-6636(82)90022-9
- Kovalyshen, Y., Sarout, J., Dautriat, J., Maney, B., & Lebedev, M. (2020). Ultrasonic characterization of anisotropic rocks: Impact of transducers' size and geometry on data interpretation. *Geophysics*, 85(4), C99–C105. https://doi.org/10.1190/GEO2019-0083.1
- Le Ravalec, M., & Guéguen, Y. (1996). High- and low-frequency elastic moduli for a saturated porous/cracked rock–Differential self-consistent and poroelastic theories. *Geophysics*, 61(4), 1080–1094. https://doi.org/10.1190/1.1444029
- Lockner, D. A., & Beeler, N. M. (2003). Stress-induced anisotropic poroelasticity response in sandstone. In *Electronc proc. 16th ASCE Engin. Mech. Conf.* (pp. 1–13). U. Washington.
- Lockner, D. A., & Byerlee, J. (1977). Acoustic emission and creep in rock at high confining pressure and differential stress. *Bulletin of the Seismological Society of America*, 67(2), 247–258. https://doi.org/10.1785/bssa0670020247
- Lockner, D. A., Byerlee, J. D., Kuksenko, V., Ponomarev, A., & Sidorin, A. (1991). Quasi-static fault growth and shear fracture energy in granite. Nature, 350(6313), 39–42. https://doi.org/10.1038/350039a0
- Lockner, D. A., & Stanchits, S. (2002). Undrained poroelastic response of sandstones to deviatoric stress change. *Journal of Geophysical Research*, 107(B12), https://doi.org/10.1029/2001JB001460
- Lokajíček, T., Vasin, R., Svitek, T., Petružalek, M., Kotrlý, M., Turková, I., et al. (2021). Intrinsic elastic anisotropy of westerly granite observed by ultrasound measurements, microstructural investigations, and neutron diffraction. *Journal of Geophysical Research*, 126. https://doi.org/10.1029/2020JB020878
- Martin, C. D., & Chandler, N. A. (1994). The progressive fracture of Lac du Bonnet granite. International Journal of Rock Mechanics and Mining Science & Geomechanics Abstracts, 31(6), 643–659. https://doi.org/10.1016/0148-9062(94)90005-1
- McBeck, J., Ben-Zion, Y., & Renard, F. (2022). Volumetric and shear strain localization throughout triaxial compression experiments on rocks. *Tectonophysics*, 822, 229181. https://doi.org/10.1016/j.tecto.2021.229181
- Mitchell, T. M., & Faulkner, D. R. (2008). Experimental measurements of permeability evolution during triaxial compression of initially intact crystalline rocks and implications for fluid flow in fault zones. *Journal of Geophysical Research*, 113(B11). https://doi.org/10.1029/20081B005588
- Passelègue, F. X., Brantut, N., & Mitchell, T. M. (2018). Fault reactivation by fluid injection: Controls from stress state and injection rate. Geophysical Research Letters, 45(23), 12837–12846. https://doi.org/10.1029/2018GL080470
- Paterson, M. S., & Wong, T. F. (2005). Experimental rock deformation The brittle field (2nd ed.). Springer-Verlag.
- Peltzer, G., Rosen, P., Rogez, F., & Hudnut, K. (1998). Poroelastic rebound along the Landers 1992 earthquake surface rupture. *Journal of Geophysical Research*, 103(B12), 30131–30145. https://doi.org/10.1029/98jb02302
- Pimienta, L. X., Borgomano, J. V. M., Fortin, J., & Guéguen, Y. (2016). Modelling the drained/undrained transition: Effect of the measuring method and the boundary conditions. Geophysical Prospecting, 64(4), 1098–1111. https://doi.org/10.1111/1365-2478.12390
- Pimienta, L. X., Fortin, J., & Guéguen, Y. (2015a). Bulk modulus dispersion and attenuation in sandstones. *Geophysics*, 80(2), D111–D127. https://doi.org/10.1190/GEO2014-0335.1
- Pimienta, L. X., Fortin, J., & Guéguen, Y. (2015b). Experimental study of Young's modulus dispersion and attenuation in fully saturated sandstones. *Geophysics*, 80(5), L57–L72. https://doi.org/10.1190/GEO2014-0532.1

ELSIGOOD ET AL. 22 of 23

- Sayers, C., & Kachanov, M. (1995). Microcrack-induced elastic wave anisotropy of brittle rocks. *Journal of Geophysical Research*, 100(B3), 4149–4156. https://doi.org/10.1029/94jb03134
- Scholz, C. H., & Kranz, R. L. (1974). Notes on dilatancy recovery. *Journal of Geophysical Research*, 79(14), 2132–2135. https://doi.org/10.1029/jb079i014p02132
- Schubnel, A., & Guéguen, Y. (2003). Dispersion and anisotropy of elastic waves in cracked rocks. *Journal of Geophysical Research*, 108(B2). https://doi.org/10.1029/2002JB001824
- Schubnel, A., Nishizawa, O., Masuda, K., Lei, X. J., Xue, Z., & Guéguen, Y. (2003). Velocity measurements and crack density determination during wet triaxial experiments on Oshima and Toki granites. *Pure and Applied Geophysics*, 160, 869–887. https://doi.org/10.1007/978-3-0348-8083-1
- Shafiro, B., & Kachanov, M. (1997). Materials with fluid-filled pores of various shapes: Effective elastic properties and fluid pressure polarization. *International Journal of Solids and Structures*, 34(27), 3517–3540. https://doi.org/10.1016/s0020-7683(96)00185-0
- Skempton, A. W. (1954). The pore-pressure coefficients A and B. Géotechnique, 4, 143-147. https://doi.org/10.1680/geot.1954.4.4.143
- Stevens, J. L., & Holcomb, D. J. (1980). A theoretical investigation of the sliding crack model of dilatancy. *Journal of Geophysical Research*, 85(B12), 7091–7100. https://doi.org/10.1029/jb085ib12p07091
- Thomsen, L. (1986). Weak elastic anisotropy. Geophysics, 51(10), 1954–1966. https://doi.org/10.1190/1.1442051
- Walsh, J. B. (1965a). The effect of cracks in rocks on Poisson's ratio. *Journal of Geophysical Research*, 70(20), 5249–5257. https://doi.org/10.1029/iz070i020p05249
- Walsh, J. B. (1965b). The effect of cracks on the compressibility of rock. *Journal of Geophysical Research*, 70(2), 381–389. https://doi.org/10.1029/jz070i002p00381
- Wang, H. F. (1997). Effects of deviatoric stress on undrained pore pressure response to fault slip. *Journal of Geophysical Research*, 102(B8), 17943–17950. https://doi.org/10.1029/97jb01358
- Wang, H. F. (2000). Theory of linear poroelasticity with application to geomechanics and hydrogeology. Princeton University Press.
- Wong, T. F. (2017). Anisotropic poroelasticity in a rock with cracks. *Journal of Geophysical Research*, 122(10), 7739–7753. https://doi.org/10.1002/2017JB014315
- Zoback, M. D., & Byerlee, J. D. (1975a). The effect of cyclic differential stress on dilatancy in westerly granite under uniaxial and triaxial conditions. *Journal of Geophysical Research*, 80(11), 1526–1530. https://doi.org/10.1029/jb080i011p01526
- Zoback, M. D., & Byerlee, J. D. (1975b). The effect of microcrack dilatancy on the permeability of westerly granite. *Journal of Geophysical Research*, 80(5), 752–755. https://doi.org/10.1029/jb080i005p00752
- Zoback, M. D., & Healy, J. H. (1992). In situ stress measurements to 3.5 km depth in the Cajon Pass scientific research borehole: Implications for the mechanics of crustal faulting. *Journal of Geophysical Research*, 97(B4), 5039–5057. https://doi.org/10.1029/91jb02175

ELSIGOOD ET AL. 23 of 23